Ordering and Melting of Block Copolymer Spherical Domains in 2 and 3 Dimensions

Rachel A. Segalman,[†] Alexander Hexemer,[‡] Ryan C. Hayward,[†] and Edward J. Kramer*[,†,‡]

Departments of Chemical Engineering and Materials, University of California, Santa Barbara, Santa Barbara, California 93106

Received August 22, 2002

ABSTRACT: We observe that a 2-D single crystalline layer of spherical diblock copolymer domains templated by lateral substrate topology melts via a continuous defect generation process, similar to that predicted by Kosterlitz, Thouless, Halperin, Nelson, and Young. The layer of spheres is allowed to order (or disorder) by annealing for 72 h at a given temperature, T, that corresponds to a given χN_{min}, where χ is the temperature-dependent Flory−Huggins parameter and N_{min} is the number of mers in the minority block. The structure of the layer is revealed by imaging the ion beam etched film using scanning force microscopy. If $\chi N_{min} > 9$, the film is polycrystalline and the system appears to be kinetically trapped. For $9 > \chi N_{min} > 7.4$, we observe that the film is a single crystal with quasi-long-range order and few defects, as expected for the 2-D crystal. As T is increased further (χN_{min} is decreased), we observe that defects are generated, predominantly dislocation pairs and other dislocation clusters with no long-range strain field. Increasing numbers of free dislocations are observed as χN_{min} is decreased further. This dislocation unbinding produces a hexatic phase which has quasi-long-range orientational order but only short-range translational order. At still higher T ($\chi N_{min} = 7.2$), the dislocations unbind into +60° and −60° free disclinations to form an isotropic 2-D liquid of block copolymer micelles. This hexatic to liquid transition occurs at a χN_{min} below that corresponding to the bulk lattice disordering−ordering transition as measured by small-angle X-ray scattering.

Introduction

The ability of block copolymers to order into nanometer-sized domains makes them uniquely suited for patterning large areas with dense arrays of small features for further use in nanolithography or the templating of inorganic materials for microelectronics applications. For example, block copolymer films have been used as masks for reactive ion etching (RIE) pattern transfer to underlying substrates to produce densely arranged features for use in semiconductor and magnetic storage applications.[1−5] The block copolymer nanometer domains have also served as sites for the inorganic synthesis of a variety of nanowires[6,7] and metallic dots.[8,9] For all of the above applications, the block copolymer self-assembly route is attractive because it allows patterning on sub-optical lithographic (sub-100 nm) length scales. Most commonly, the domain orientation in cylinder and lamella forming diblock copolymers is controlled by using external fields such as electrical[10,11] and surface interactions[12,13] and by controlling island/hole topography with chemically patterned substrates.[14] Nealey et al. have also shown that, by chemically patterning the substrate on a nanometer scale, it is possible to directly pattern the overlying nanodomains of block copolymer.[15,16] Recently, we have shown that it is possible to achieve single crystal films of spherical domains via topographical templating on a much larger scale.[17]

All of these efforts have focused on controlling domain orientation and occasionally on controlling actual domain placement via the use of external forces at an arbitrarily chosen temperature. It is necessary, however, to balance the kinetics of pattern formation with the thermodynamics of block copolymer segregation in order to achieve even higher degrees of order. For instance, Yokoyama et al. demonstrated that, in the three-dimensional case of very thick films, the interplay between kinetics and thermodynamics controls the extent to which layers of spheres stack with registry to the surface.[18] The degree to which the two blocks will segregate thermodynamically is proportional to χN_{min}, where χ is the temperature-dependent Flory−Huggins parameter and N_{min} is the length of the smaller of the two blocks. The lower the temperature, the stronger the driving force causing the two blocks to segregate and order. Diffusion, however, becomes exponentially slower as χN_{min} increases since $D \sim D_0 \exp(-\alpha\chi N_{min})$.[19,20] At lower temperatures, the polymer may not diffuse fast enough to allow rearrangement of spherical domains into a structure with long-range order. The interplay between these opposite dependences on χN_{min} results in an optimum annealing condition. Similarly, Kim et al. demonstrated that grain growth rates can be optimized by correctly tuning the quench depth of a bulk sample from the order−disorder temperature (ODT) due again to an interplay between thermodynamic driving forces and frictional resistance.[21]

The properties of block copolymer melts in the vicinity of the ODT have been intensely studied over the past two decades. Experiments,[18,22−29] computer simulations,[30] and theoretical developments[31,32] have led to a better understanding of how an asymmetric copolymer, which forms spherical micelles ordered on a body-centered-cubic (bcc) lattice at large χN_{min} disorders as χN_{min} is decreased. In contrast to symmetric block copolymers whose lamellar microdomains disorder directly into the homogeneous state through a single ODT,

[†] Department of Chemical Engineering.
[‡] Department of Materials.
* To whom correspondence should be addressed: e-mail edkramer@mrl.ucsb.edu; Tel (805) 893-4999.

10.1021/ma021367m CCC: $25.00
Published on Web 04/03/2003

these asymmetric block copolymers appear to go through a series of transitions from spheres on an ordered lattice to disordered spheres to a homogeneous state. As of yet, it is unclear how many distinct equilibrium phases occur during the transition, but a popular terminology set views the system as progressing through two first-order transitions during heating: first the spheres on an ordered lattice disorder into randomly packed micelles (lattice disorder−order transition (LDOT)) and then disorder completely into disordered chains (demicellization/micellization transition (DMT)).[23,24] The discussion as to whether the DMT is a distinct first-order transition or whether there is a continuous change in micellar concentration and size leading to a critical micelle temperature (CMT) is ongoing.[22,31]

The LDOT, where the ordered phase transforms to a phase of disordered spheres with short-range liquidlike order, can viewed as a simple melting transition from an ordered array of objects to one that is disordered. In lower dimensionalities, the situation is expected to be more complicated. In 1-D and 2-D, the translational order of the crystalline phase is diminished by thermally excited long wavelength phonons so that true long-range translational order is not possible. Instead, a 1-D crystal will only have short-range translational order,[33,34] and a 2-D crystal will have only quasi-long-range translational order.[35,36] Kosterlitz, Thouless, Halperin, Nelson, and Young[37−41] predict that melting in 2-D crystals is a continuous transition driven by the thermal generation of defects. It is useful, in this description, to distinguish between translational order, frequently parametrized by a pair correlation function, and orientational order, defined as the 6-fold symmetry of the array at any point. A two-dimensional crystal is expected to first lose its translational order on heating and then only at a higher temperature lose its orientational order. This leads to the prediction of a two-stage continuous melting transition instead of the first-order transition observed in three dimensions. As predicted by Halperin and Nelson, the first stage of this transition is characterized by a loss in translational order due to the dissociation of bound dislocation pairs to form a hexatic phase.[39,40] The hexatic phase has only short-range translational order but quasi-long-range orientational order. In the second stage of melting, individual dislocations dissociate into their component disclinations, destroying order and forming a true liquid. The liquid is characterized as having only short-ranged translational and orientational order.

The conditions under which this theory predicts the results of simulations and experiments have been the subject of active debate over the past several decades.[42,43] While the continuous hexatic to liquid melting transition has been observed in some simulations,[44−49] other simulations[50,51] have failed to reveal it, and there is a continuing discussion on the effects of simulation size.[52−54] Experimentally, two-dimensional melting through a hexatic phase has been reported in polymeric colloids,[55−60] paramagnetic colloids,[61] and magnetic bubble arrays in garnet films.[62,63] Though the classic KTHNY theory is the most popular theory of two-dimensional melting, it has been demonstrated that, by changing the interactions between the spheres (in particular, changing the charging condition of colloids), it is possible to change the sequence of melting events. Chui[64] demonstrated that this transition may be preempted by grain boundary induced melting. Blandon and Frenkel[50] simulated and Marcus and Rice[59,60] experimentally observed a first-order crystal to hexatic transition followed by a first-order hexatic to liquid transition for an uncharged, sterically stabilized colloidal array in which the particle−particle interaction has a hard core and a very short-range attraction. Chou and Nelson have since extended KTHNY theory to include these findings.[65] It was later shown also that uncharged silica spheres melt via a first-order transition to a liquid without a hexatic intermediate.[66]

Though the 2-D colloids represent an interesting model system, the shape of the colloids is rigid, and the melting is driven by changes in the volume fraction of colloids in the system. In a block copolymer system, the spheres may deform and change size via the diffusion of block copolymer chains between nanodomains. The magnetic bubble system, however, is a closer analogy since the bubbles are not of fixed size or volume, though the melting in this case is also not driven via temperature but rather by modifying the surrounding magnetic field such that the number density of bubbles of reversed magnetization in the garnet is also modified. Recently, the melting of a 2-D lattice of spherical nanodomains of block copolymers has also been observed in a polystyrene−poly(ethylene-*r*-propylene) diblock copolymer system by Angelescu et al.[67]

In previous studies, we have demonstrated that a single layer of block copolymer spheres on a planar silicon oxide surface is polycrystalline. By imposing topographical confinement, these spheres can be induced to order into single crystalline arrays as broad as 5 μm in dimension. In this paper, we will show that it is necessary to balance the thermodynamic driving force for phase segregation with the kinetic limitations for nanodomain rearrangement in a block copolymer system in order to reach the best order possible. Even under the best possible conditions, however, we find that true long-range translational order cannot be created in a 2-D block copolymer layer, in agreement with the general theoretical predictions outlined above.

Further, we will demonstrate that the mechanism by which a single layer of spheres disorders is analogous to the two-dimensional melting previously observed in other systems by studying the defect character of single crystalline block copolymer sphere arrays. We will show that this melting is described by the KTHNY theory for two-dimensional melting by analyzing the orientational and translational order of the block copolymer array under a variety of annealing conditions. Finally, we will demonstrate that the hexatic to liquid melting temperature is depressed when compared to the 3-D LDOT temperature (T_{LDOT}).

Experimental Section

Polystyrene-*b*-(2-vinylpyridine) (PS−PVP) with $N = 670$ and $f_{PVP} = 0.129$, where N is the total degree of polymerization of the block copolymer and f_{PVP} is the mole fraction of PVP mers, was synthesized via anionic polymerization as previously documented.[18] In the bulk, this material self-assembles into spherical PVP cores 9 nm in diameter surrounded by PS coronae to form bcc arrays with a (110) plane spacing of 27 nm.

Small-Angle X-ray Scattering. SAXS was performed at the Material Research Laboratory X-ray Facility at UCSB on a 0.8 mm thick, melt-pressed sample of PS−PVP. This sample was preannealed at 200 °C in high vacuum ($P < 10^{-6}$ Torr). The sample was then compressed between two sheets of Kapton and two copper washers and placed in an Instec heat stage which was then placed in the SAXS beamline. The heat

stage was operated at a constant overpressure of high-purity N_2. Temperature was varied from 160 to 305 °C with an accuracy of ±1 °C, and the sample reached each temperature within 30 s. At each temperature step, the sample was annealed for 30 min prior to X-ray exposure to make sure that it was in thermal equilibrium. Scattering data were then collected for 31 min. Copper Kα radiation with wavelength 1.54 Å was generated by a fine focus (0.2 mm) Rigaku rotating anode generator. The beam line was configured with a spot size of approximately 1 mm × 1 mm which was transmitted through the Kapton windows of the cell. Scattering patterns were collected on a Bruker HI-STAR multiwire area detector located 1.5 m from the sample.

Dynamic Secondary Ion Mass Spectroscopy (SIMS). Silicon substrates were obtained from Cypress Semiconductor Corp. (Minneapolis, MN), and a 300 nm thick layer of silicon oxide was deposited on the wafer via electron beam evaporation. A 10 μm thick film of PS−PVP was formed by allowing a drop of 10% PS−PVP/toluene solution on the substrate to evaporate in a toluene vapor environment for 30 h. The samples were then annealed in high vacuum ($<10^{-6}$ Torr) at the designated temperature for 24 h. Prior to SIMS analysis, a sacrificial layer of deuterated PS thin film (~60 nm thick) was spun-cast onto a glass microscope slide, floated off onto a distilled water bath, and picked up onto the PS−PVP specimen surface. This sacrificial layer was used to calibrate the etch rate of the SIMS.

Depth profiles were obtained from a Physical Electronics 6650 dynamic SIMS using a 3 keV, 50 nA beam of O_2^+ ions that was rastered over a 300 μm × 300 μm area. Charge neutralization was achieved with a 0.6 eV defocused electron beam. The SiO_2 substrate layer serves to insulate the overlying polymer layer so that charge neutralization conditions using a low-energy electron gun in the SIMS crater do not change as the crater approaches the polymer/substrate interface.

Sample Preparation of 2-D Arrays. A 30 nm thick layer of silicon oxide was deposited on silicon wafers via electron beam evaporation. The substrate was then patterned with a series of long (1 mm) mesas and wells with heights of 30 nm via standard photolithography and chemical etching with hydrofluoric acid. These mesas and wells ranged in width from 1 to 10 μm. A 1.5 nm thick native oxide layer was then allowed to regrow on all etched surfaces.

Thin films of PS−PVP were spun-cast from dilute (~1%) toluene solution directly onto the patterned substrates or onto glass microscope slides. In the latter case, the slides were slowly immersed in deionized water immediately after spin-coating. The intrinsic layer of surfactant on the glass surface released the films to the air/water interface where they were retrieved on top of patterned silicon substrates. There was no noticeable difference in the final films produced by the two techniques after final ordering.

All samples were annealed at a designated temperature in high vacuum ($<10^{-6}$ Torr) for 72 h to allow ordering. The samples were then quenched to below the glass transition temperature (~100 °C) to lock in the structure. This resulted in a 20 nm PVP brush at the silicon surface followed by a layer of PVP cores surrounded by PS coronae as illustrated schematically in Figure 1.

Islands and holes form when the original, spun-cast film thickness does not match a natural thickness, h, given approximately by

$$h = \alpha n + \beta \qquad (1)$$

where α is the thickness of a layer of spheres (27 nm), β is the thickness of a layer of PS−PVP brush absorbed on the silicon oxide surface (20 nm), and n is an integer value. When the film is slightly thicker than h, islands containing excess material form. To reduce their line tension, they coarsen by accumulating near the hard edge of the well. This configuration effectively decreases the width of the well to accommodate the excess material without any increase in island edge-line length. Similarly, when the film is slightly thinner than h, holes form in the single layer of spheres to reveal the brush.

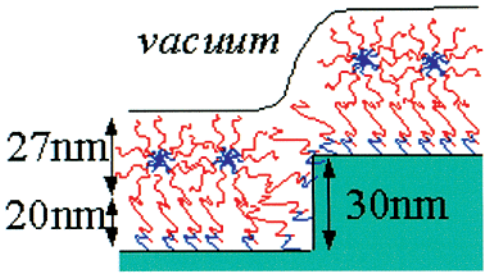

Figure 1. After annealing on a topographically patterned silicon substrate, a 20 nm PS−PVP brush with a single layer of spheres is observed. The material on the raised areas (mesas) is confined by the presence of vacuum surfaces on either side while the material in the wells is confined by the presence of the hard silicon steps on either side. Both forms of confinement lead to an epitaxial ordering of the spheres.

This brush is preferentially formed on the outer edges of the mesa to effectively decrease the width of the mesas. The kinetics of this island/hole formation and further details on the structure of the islands and holes will be presented elsewhere.[68] For the purposes of the following work, great care was taken to cast the film to be exactly 47 nm thick (one sphere layer and one brush) on all surfaces.

The top surface of the film appears flat on a 5 nm height scale, indicating that the PS coronae conform to a planar surface. The lateral location of the PVP cores was revealed by etching to the midplane of the layer of spheres using SIMS. SIMS etching was accomplished using the same instrument detailed above, but etching was accomplished by rastering a 1 kV beam of O_2^+ ions over a 0.09 mm^2 crater. Charge neutralization was accomplished using a static, defocused 1 keV electron beam centered on the crater being etched by the SIMS. Negative ions of H, CN, and Si were monitored as a function of time. The etch was stopped at a local maximum in the CN^- signal, indicating the location of the midplane of a layer of spheres. The polar PVP cores are etched slightly faster than the surrounding PS matrix resulting in a 1 nm height contrast, which could be imaged with tapping mode scanning force microscopy (SFM) performed on a Digital Instruments MultiMode AFM.

The SFM was allowed to scan for several hours prior to image capture to ensure the best possible thermal equilibration of the piezo tube and to reduce the resulting stretching/compression of the image. Several successive images of the same region were then captured. It was noticed that the SFM alternately compressed and stretched the image in the slow scan direction of successive scans due to drifting of the piezo. Small amounts of drift were associated not only with previous changes in scan location and scan size but also with the presence of drafts and gradients in ambient temperature and were found to be unavoidable. The 2-dimensional Fourier transform was computed for each digital image, and it was noticed that the distances to the first-order ring in the fast scan direction stayed constant while the distance to the first-order ring in the slow scan direction was either compressed or stretched. Each image was corrected for this distortion by inversing the contraction or expansion (by stretching or compressing the digital image in the slow scan direction) so that the first-order ring was round (equally spaced from the origin in all directions). This method of image correction removed all artificial distortion in the hexagonal lattices.

The SFM scans of the etched films contained some long wavelength background (see for example Figure 2a). Image contrast enhancement was necessary to facilitate the automated detection of all sphere centers (observed as dark areas surrounded by bright). Though a common method of enhancing a periodic pattern is to apply a Fourier filter, great care must be taken in filtering images of lattices with defects to avoid introducing artifacts. Defects in periodic arrays such as grain boundaries and dislocations can be considered perturbations of the lattice in the sense that most of the image retains the lattice periodicities.[69] The images were therefore manipulated

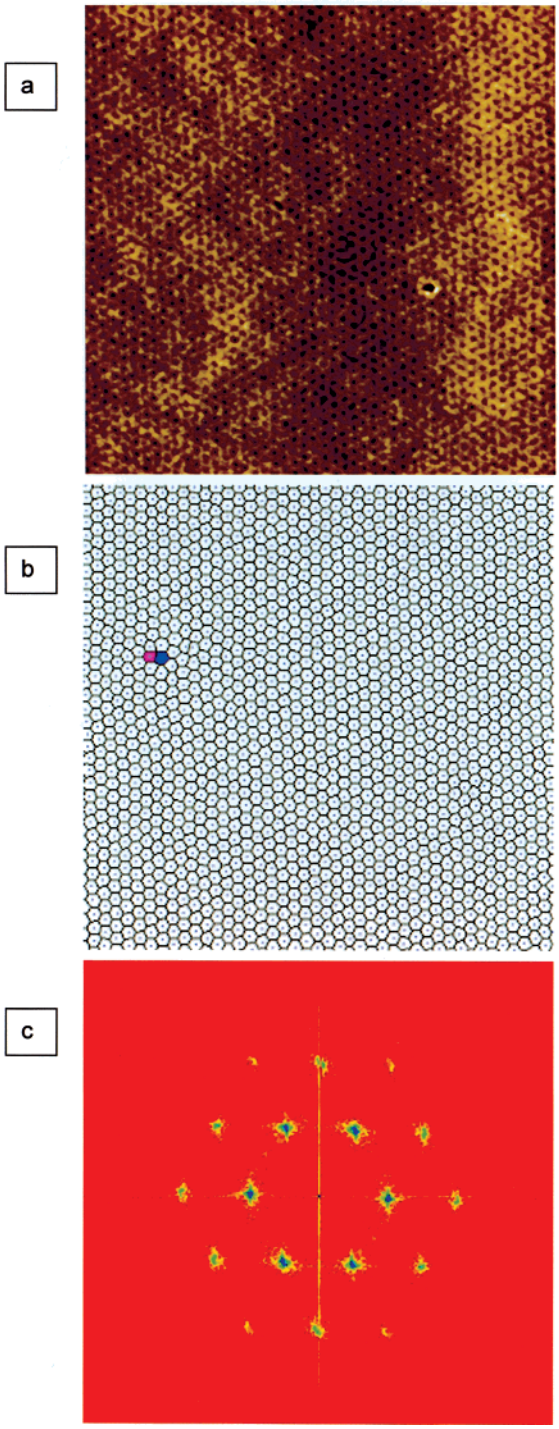

Figure 2. The 1.5 μm square region annealed at $\chi N_{PVP} = 9.1$ (180 °C) for 72 h on a mesa with the vacuum edge just to the left of the image. (a) SFM micrograph of the region after etching with SIMS. The dark areas are lower than the bright such that the total height scale (from dark to bright) is 5 nm. The SIMS preferentially etches the PVP cores so they appear as 1 nm dimples (dark) in the brighter matrix. The close-packed rows are aligned parallel to the edge and are very straight, indicating that the single grain is near perfect. (b) Voronoi diagram constructed from the sphere center locations. Six-fold-coordinated sites are unshaded while 5-fold sites are magenta and 7-fold sites are blue. The presence of one 5−7 pair indicates the presence of a single dislocation in the image. (c) Fourier transform with false color (low scattering intensities are shaded red and high intensities are blue). Six sharp first-order peaks equidistant from the center further support the view that this is a single crystalline, hexagonal grain. The presence of higher-order peaks attests to the high degree of order within the grain.

by enhancing the periodicity associated with our hexagonal array (2π/repeat spacing). This was done by convoluting the image mathematically:

$$h(x) = \int_0^x f(t)\, g(x - t)\, dt = \int_{-\infty}^{\infty} \hat{f}(\mathbf{q})\, \hat{g}(\mathbf{q})\, e^{iqx}\, dq \qquad (2)$$

where $h(x)$ is the convolved image, $f(t)$ is the original image, and $g(x-t)$ is the convolving function. This was done by taking the Fourier transform of $f(t)$, $\hat{f}(q)$, and multiplying with the transformed function, $\hat{g}(q)$, and then inverse transforming the product to create a new image, $h(x)$. For $\hat{g}(q)$, we used a Gaussian with maximum occurring at the first Fourier peak of $\hat{f}(q)$ and full width half-maximum of $2\pi/a$, where a is one lattice spacing. This width was chosen to preserve any lattice defects present in $f(t)$.

Image Pro by Media Cybernetics was then used to identify the center of every dark region which we identify as PVP cores. This generated a matrix of PVP core locations which could be used for further analysis. While close to perfect, this automated sphere finding algorithm still required some hand correction to separate closely spaced spheres (on average 4 pairs per 1.5 μm square SFM image).

Results and Discussion

Defect Concentrations and Phenomonological Observations of 2-D Melting. A useful overall picture of the melting phenomenon can be attained by qualitatively observing the changes in the crystalline array as a function of annealing temperature. In particular, it is useful to identify the presence of grain boundaries, dislocations, and other lattice defects through analysis of SFM images of the layer of spheres. Figure 2a shows a representative SFM micrograph of a 1.5 μm square region of spheres ordered at 180 °C ($\chi N_{PVP} = 9.1$) for 72 h, then quenched to room temperature, and etched with SIMS. By eye, it is obvious that the close-packed lines of the array are generally straight and persist throughout the scan, indicating that a single, near perfect crystal is present. The corresponding Voronoi diagram is presented in Figure 2b and aids in observing the close-packed rows. Figure 2c is a 2-dimensional Fourier transform calculated from the sphere center position matrix generated by Image Pro. It has been color-coded with a spectrum from red to yellow to blue to designate low- to medium- to high-intensity regions, respectively. The six sharp first-order peaks as well as sharp second- and third-order peaks visible in this transform further indicate the presence of a single, well-formed hexagonal grain.

It is useful to visualize the presence of crystal defects through a Voronoi diagram which is constructed by drawing bonds connecting a sphere with all of its neighbors. The perpendicular bisectors of these bonds intersect to form a polygon. The polygon has a number of sides equal to the number of nearest neighbors of the sphere in the center. These polygons can be used to identify a variety of lattice defects, as seen in Figure 3. The 6-fold-coordinated sites are uncolored and appear as white hexagons while 5-fold-coordinated species (5's) are displayed as blue pentagons and 7-fold-coordinated sites (7's) are displayed as magenta heptagons. An isolated dislocation is shown in Figure 3a, with both an SFM image and its corresponding Voronoi diagram with its Burgers vector shown in blue. The core of the dislocation, seen as a 5−7 pair in the Voronoi diagram, is the point where the two extra half lines of material (indicated by red lines) intersect. The 5's represent points at which a 60° segment of symmetry has been

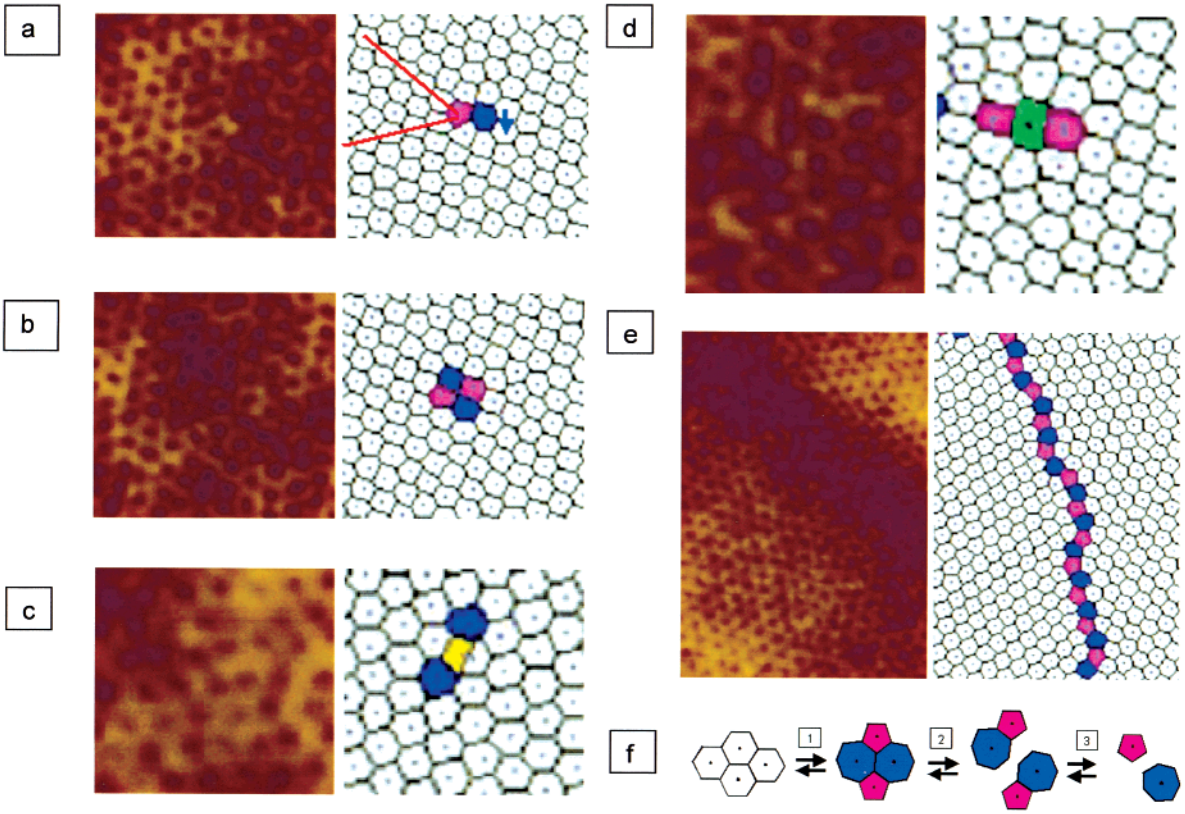

Figure 3. Defects in 2-D diblock copolymer crystals for which Voronoi diagrams were constructed using same color coding as Figure 2 and their corresponding unfiltered SFM images: (a) Individual dislocation: A paired pentagon and heptagon (5−7 pair) occurs when two extra half rows of spheres (shown as red lines in the Voronoi diagram) intersect at the core of the dislocation. This defect has a Burgers vector in the direction of the indicating arrow. (b) Dislocation pair: In the Voronoi construction this is seen as a quadrapole of two pentagons and two heptagons (two 5's and two 7's). This dislocation pair has no net Burgers vector. (c, d) Other defects with no net Burgers vector: As the system melts, other defect forms can be created as defects glide and climb into each other. (c) 7−4−7 groupings are interstitial spheres (squares are colored yellow). (d) Vacancies are frequently observed as 5−8−5 groupings (octagons are colored green). (e) A grain boundary is seen as a string of dislocations. This is a 30° grain boundary, corresponding to largest angular mismatch possible and the highest density of 5−7 pairs. (f) Dislocation-mediated melting: A dislocation pair may be formed in equilibrium by the conversion of four hexagons (6's) into a pair of dislocations (two 5's and two 7's) with little mass movement of material and zero net Burgers vector (step 1). These dislocations (5−7 pairs) may then climb and glide away from each other in step 2. Finally, each dislocation may unbind into disclinations (individual 5's and 7's) in step 3.

removed and are therefore actually −60° disclinations. The 7-coordinate sites, correspondingly, are +60° disclinations. A pair of disclinations forms the core of a dislocation. Figure 2b indicates that for a sample annealed at 180 °C for 72 h only one dislocation is present in this arbitrary 2.25 μm^2 area. The stress and strain fields of the dislocation decrease as $1/r$, where r is the distance away from the core. The elastic energy of the dislocation, E_{el}, associated with the lattice strain within a circle of radius R is proportional to $\ln(R)$, to which is added the energy of the core region, E_{core}. The lattice strain energy can be reduced by the presence of another dislocation of opposite Burgers vector at a distance of $2x < R$ so that now $E_{el} \propto \ln(x)$.[70,71] Figure 3b is such a case where two dislocations are paired so there is no net Burgers vector. In this configuration, the dislocation pair imposes no net strain field on the lattice, though there is some energy associated with each dislocation core. Parts c and d of Figure 3 are pairs of closely packed dislocations whose glide planes are offset. These correspond to an interstitial (3c) and a vacancy(3d). Neither pair has a net Burgers vector. The interstitial is seen as a 7−4 (yellow)−7 grouping while the vacancy appears as a 5−8 (green)−5 grouping. The vacancy shown is not a 6-fold symmetric hole, as one may have guessed, but has rather been crushed down to 2-fold symmetry by the interactions. This crushing has been predicted for simple repulsive pair potentials and was observed recently in colloidal experiments.[72] Figure 3e is a section of grain boundary which appears as a string of dislocations. For low-angle grain boundaries, the density of dislocations along the grain boundary is proportional to the angle between the two grains. The grain boundary shown is a 30° grain boundary, the largest angular mismatch possible, and hence contains the highest density of dislocations. At such high angles, the density of dislocations is no longer proportional to the angular mismatch.

Dislocations in two dimensions can form and annihilate spontaneously.[60,63,73] As diagrammed schematically in Figure 3f, any four spheres can form a dislocation pair with relatively little movement of core centers (step 1). This dislocation pair can dissociate, and the two dislocations can glide away from each other (step 2). Finally, each dislocation can then unbind into its component disclinations (step 3). The progression of these steps from left to right is the defect-mediated melting transition, as described by KTHNY theory. Step 2, the creation of dislocations, creates a hexatic phase. Step 3, the dissociation of dislocations into component disclinations, is the hallmark of the transition of a hexatic to a liquid.

The original KTHNY theory does not take into account any dislocations in grain boundaries, because it assumes that a single, defect-free grain exists in equilibrium prior to melting. Such grain boundaries occur frequently in a layer of block copolymer spheres ordered on a flat silicon substrate. KTHNY theory also does not preclude the possibility that the E_{core} may be very small so that the crystal may become thermodynamically unstable with respect to the fluid while it is still mechanically stable. In this case, the layer may melt by spontaneous generation of grain boundaries.[43] To allow us to differentiate between these mechanisms, it is necessary to begin the melting process with a single crystalline array. We have previously demonstrated that the region near a confining structure (mesa or well as depicted in Figure 1) is epitaxially templated by the presence of the adjacent surface (vacuum or substrate) to form a single crystalline array. All melting phenomena presented in this paper were observed within a 1.5 μm wide strip near the edge of the mesa so as to ensure that grain boundaries will not occur within the field of view. In each case, 5−10 SFM images are taken at different locations along this strip so as to ensure that a large sample set was used for each temperature studied. A future paper will address the effect of topography on the melting phenomena of sphere-forming block copolymers.[74]

Upon annealing, the PS−PVP chains quickly rearrange to form 9 nm PVP cores surrounded by PS coronae within the first 10 min of the high-temperature annealing step.[68] These spheres form a polycrystalline array which will then minimize external stresses by rearranging into the preferred crystalline orientation as the prevailing grain boundary is observed to sweep away from the substrate topography edge.[75] As shown in Figure 4, after 44 h of annealing at 180 °C a single grain exists within 1.5 μm of the edge of the mesa (indicated by the six first-order peaks in the Fourier transform). Steps 1 and 2 in Figure 3f must occur in reverse as the pattern equilibrates so that two dislocations may climb and then glide together to annihilate to form a perfectly hexagonal region. This single grain in Figure 4 is defect riddled (dislocation density $\sim 5/\mu m^2$), but over the intervening 18 h these defects must annihilate to attain the state of Figure 2 (72 h anneal dislocation density ~ 1 dislocations/μm^2). This dislocation density does not appear to be affected by an even longer annealing time (up to 100 h) or by changing the thermal history of the sample (280 °C for 72 h followed by 180 °C for 72 h). We therefore assume that, after 72 h of annealing at 180 °C, the system is approaching thermal equilibrium. It has been previously demonstrated that the stacking of layers in a thick film of sphere-forming block copolymer is dependent on χN_{PVP}, where N_{PVP} is the number of monomers in the minority block and χ is the temperature-dependent Flory interaction parameter for PS−PVP:

$$\chi = -0.033 + \frac{63}{T} \qquad (3)$$

We will adhere to this nomenclature, expressing all temperatures also in terms of χN_{PVP}, where for our system $N_{PVP} = 86$.

At $\chi N_{PVP} > 9.1$ (or temperatures less than 180 °C), there is insufficient mobility in the system to allow for sphere rearrangement and grain boundary removal within a 72 h span. Figure 5 demonstrates that this

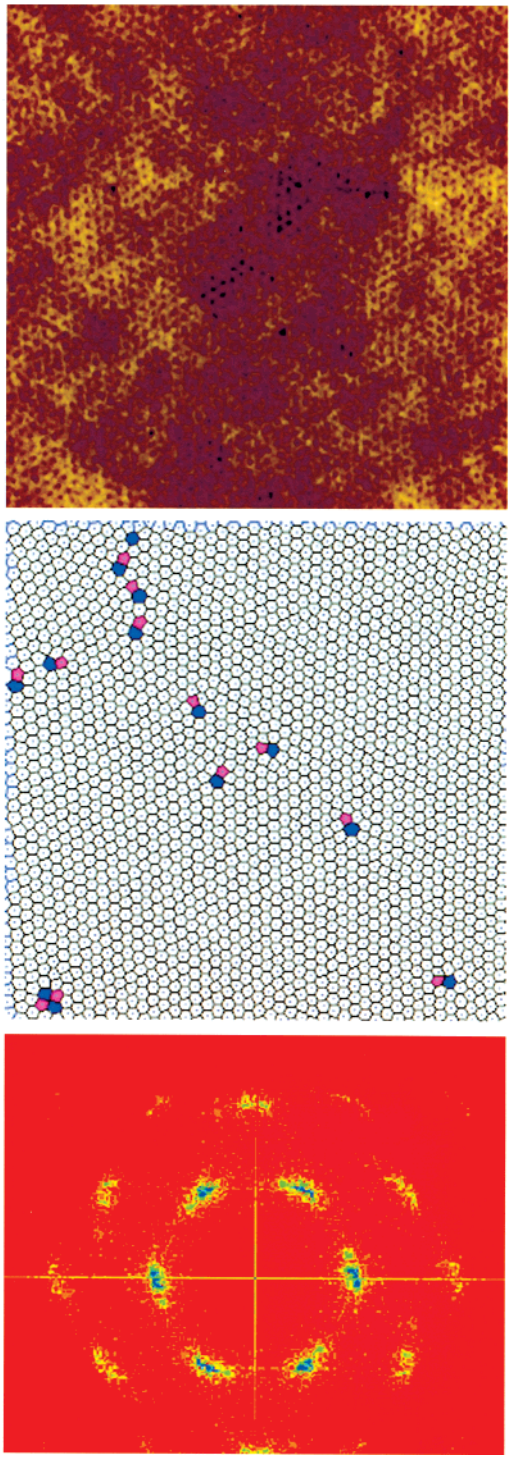

Figure 4. The 1.5 μm square region annealed at $\chi N_{PVP} = 9.1$ (180 °C) for 44 h with a mesa edge just to the left of the image. All high angle grain boundaries have been annealed out after the first 44 h of annealing, leaving a single grain with many remaining defects. The Fourier transform now shows six distinct first-order Bragg peaks, but these peaks are not sharp, indicating the presence of defects. The Voronoi diagram shows the presence of many dislocations (on average 7 dislocations/μm^2) that will annihilate over the next 28 h to yield a defect density of ~ 1 dislocations/μm^2.

system is kinetically trapped, resulting in grain boundaries within the 1.5 μm square field of view. The Voronoi diagram shows rows of dislocations indicative of grain boundaries and the Fourier transform shows 24 first-order peaks, indicating the presence of at least four grains in just this 1.5 μm square area. The number of

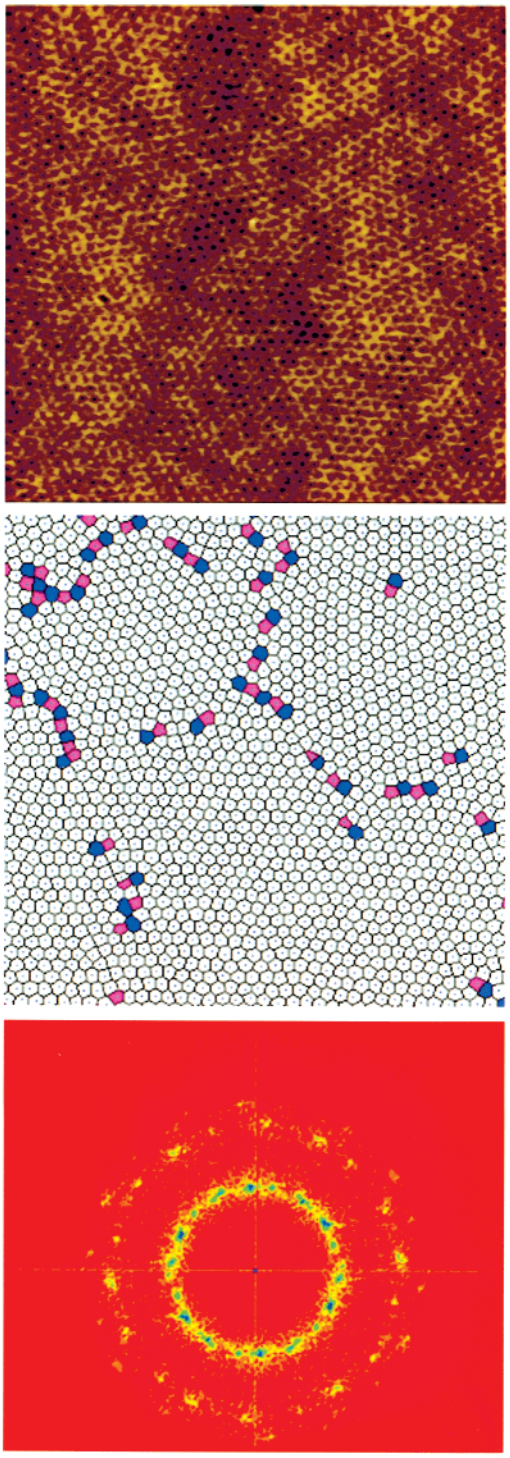

Figure 5. The PS−PVP diblock copolymer film is annealed at $\chi N_{PVP} = 10$ (150 °C) for 72 h, but there is not enough mass movement possible to allow the predominant grain to sweep across the 1.5 μm square region near the mesa edge (vacuum edge is to the left of the image). Kinetically trapped grain boundaries are visible both in the representative 1.5 μm square SFM scan shown and as strings of dislocations in the associated Voronoi construction. Similarly, the Fourier transform shows the presence of as many as 24 first-order peaks, indicating that there are at least four grains present.

isolated disclinations and dislocations (not incorporated in the grain boundaries) is minimal. It is difficult, however, to further quantify the order in this sample due to its polycrystallinity.

As temperature is increased, mobility is increased so that it is easier for grain boundaries to be eliminated.

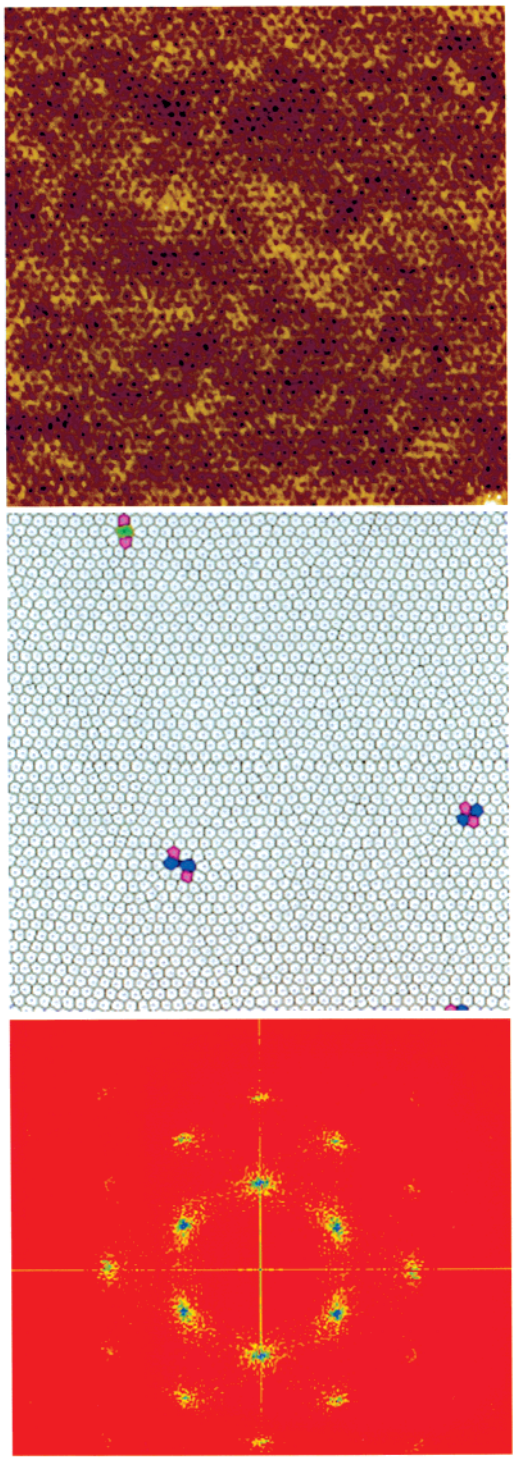

Figure 6. The PS−PVP diblock copolymer was annealed at 250 °C ($\chi N_{PVP} = 7.5$). While the 1.5 μm square SFM image and sharp first-order peaks in the Fourier transform lead us to believe this sample is a single crystal, the Voronoi construction demonstrates that more defects are present. In this image, one dislocation pair, one vacancy, and two dislocations in the process of gliding together to form another vacancy can all be observed.

For $9 < \chi N_{PVP} < 7.5$, the system is single crystalline, and very few dislocations are observed in the 1.5 μm wide area near the mesa edge (similar to Figure 2). As temperature is increased further, however, an increasing number of both isolated dislocations and dislocation clusters are observed. As seen in Figure 6, a sample annealed at 250 °C ($\chi N_{PVP} = 7.5$) has a Fourier

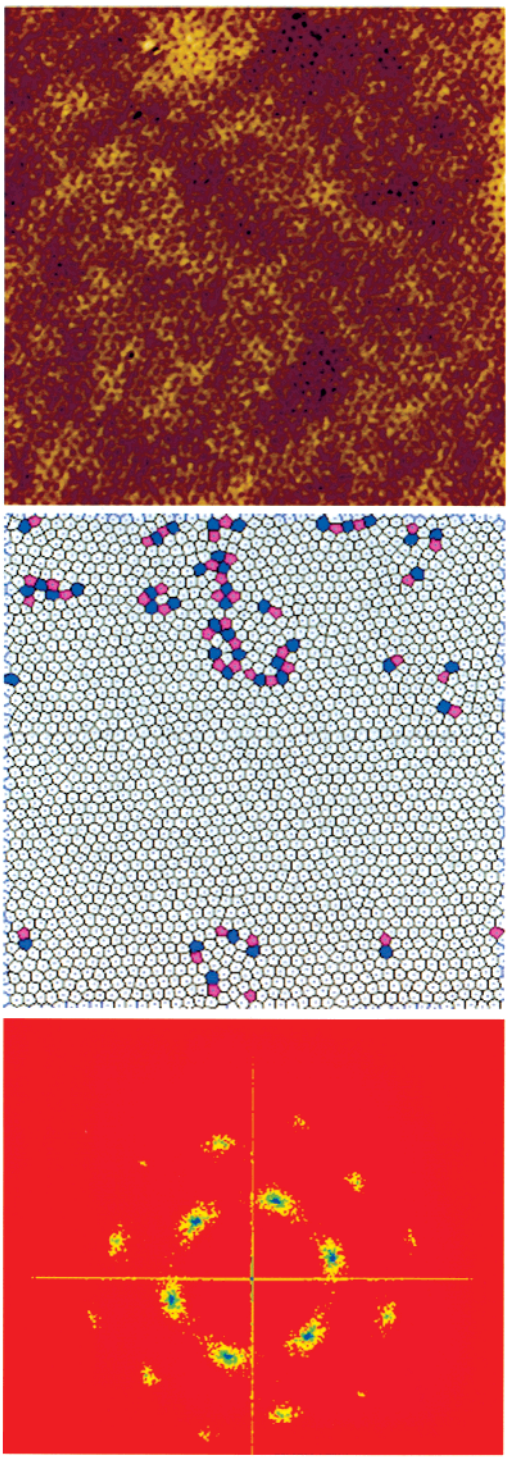

Figure 7. The PS−PVP diblock copolymer was annealed at 255 °C ($\chi N_{PVP} = 7.4$). Now the 1.5 μm square SFM image and the Voronoi diagram depict the presence of many isolated and grouped dislocations. The first-order peaks in the Fourier transform appear slightly less sharp as the system begins to melt into the hexatic phase.

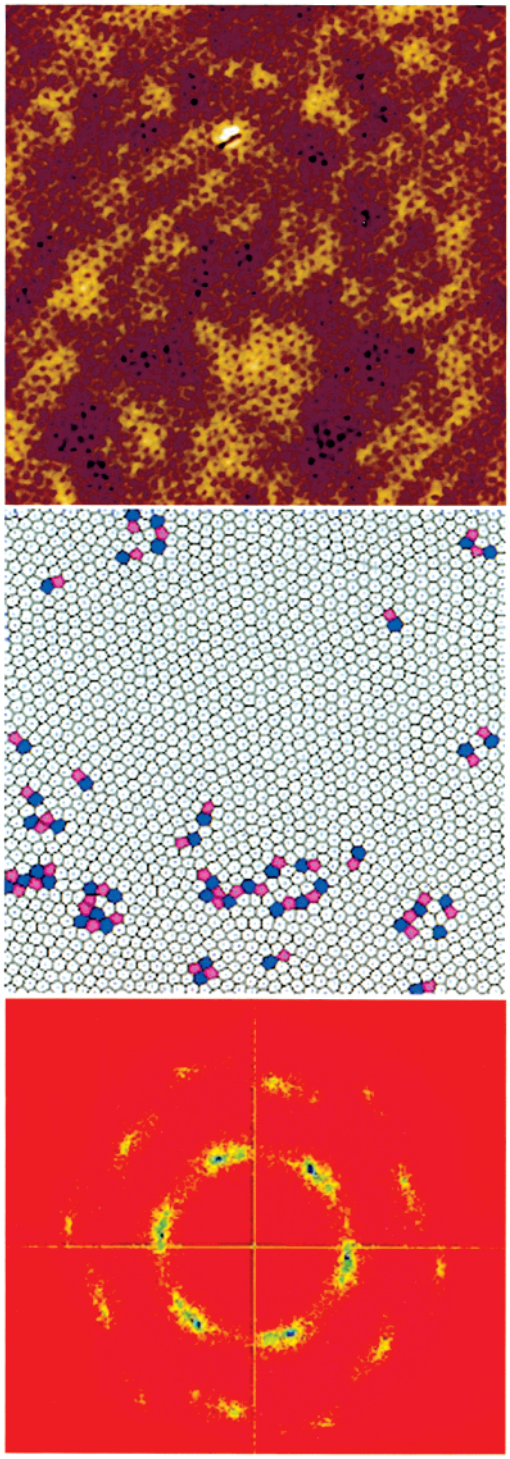

Figure 8. The PS−PVP diblock copolymer was annealed at 260 °C ($\chi N_{PVP} = 7.3$). The 1.5 μm square SFM image and associated Voronoi diagram are similar to those shown in Figure 7, except the dislocation density has increased and the dislocations appear to form larger clusters. The Fourier transform now shows a large amount of azimuthal smearing of the first-order peaks that is characteristic of the hexatic phase.

transform with relatively sharp peaks, indicating that the crystalline structure is still intact though the Voronoi diagram reveals the presence of dislocation pairs. A change, however, is evident in the Fourier transforms of samples annealed at $\chi N_{PVP} = 7.4-7.2$ (255−264 °C, Figures 7−9), which show 6-fold angular symmetry with azimuthally broadened peaks. When the annealing temperature is increased from $\chi N_{PVP} = 7.4$ to $\chi N_{PVP} = 7.3$ (250 to 260 °C), there is an obvious increase in the number of defects, but these defects are still located randomly through the image. When two dislocations of opposite Burgers vector are near each other, their elastic strain energy is low, but as they move apart it increases logarithmically with their separation, x. An increase in the dislocation density thus leads to a decrease in the elastic strain energy for introducing a

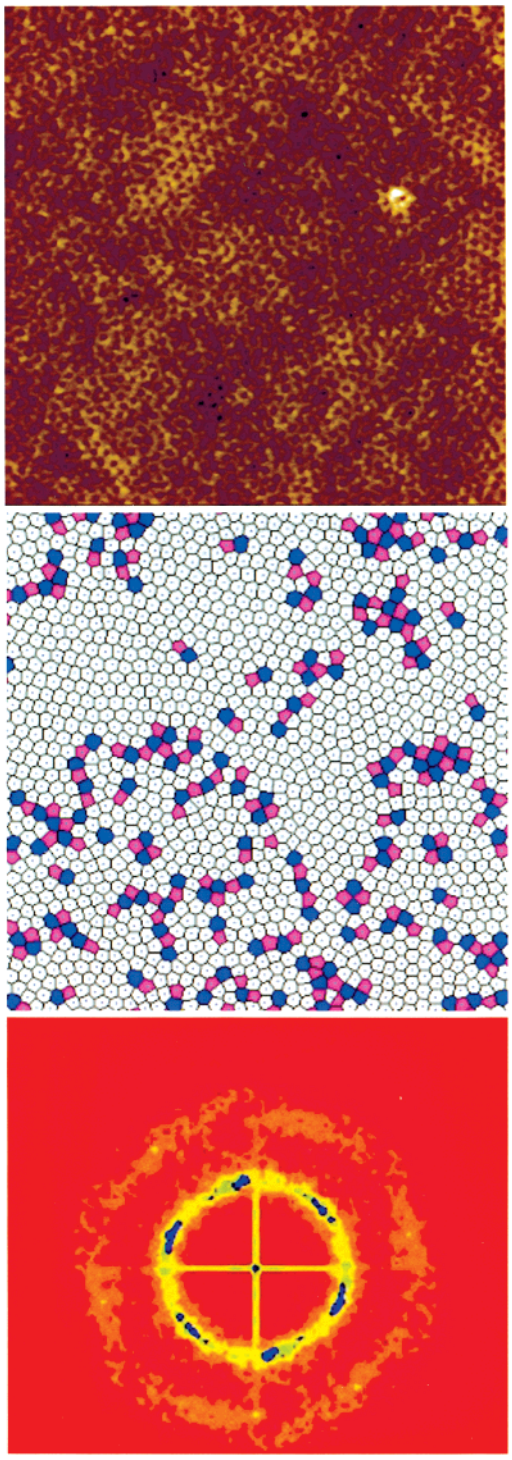

Figure 9. The PS−PVP diblock copolymer was annealed at 264 °C ($\chi N_{PVP} = 7.2$). Dislocations now span across the 1.5 μm square area visible in the SFM scan and Voronoi construction. The first-order ring in the Fourier transform is completely smeared but still shows slightly higher intensity in six evenly spaced positions in the ring, indicating that some orientational order is still present.

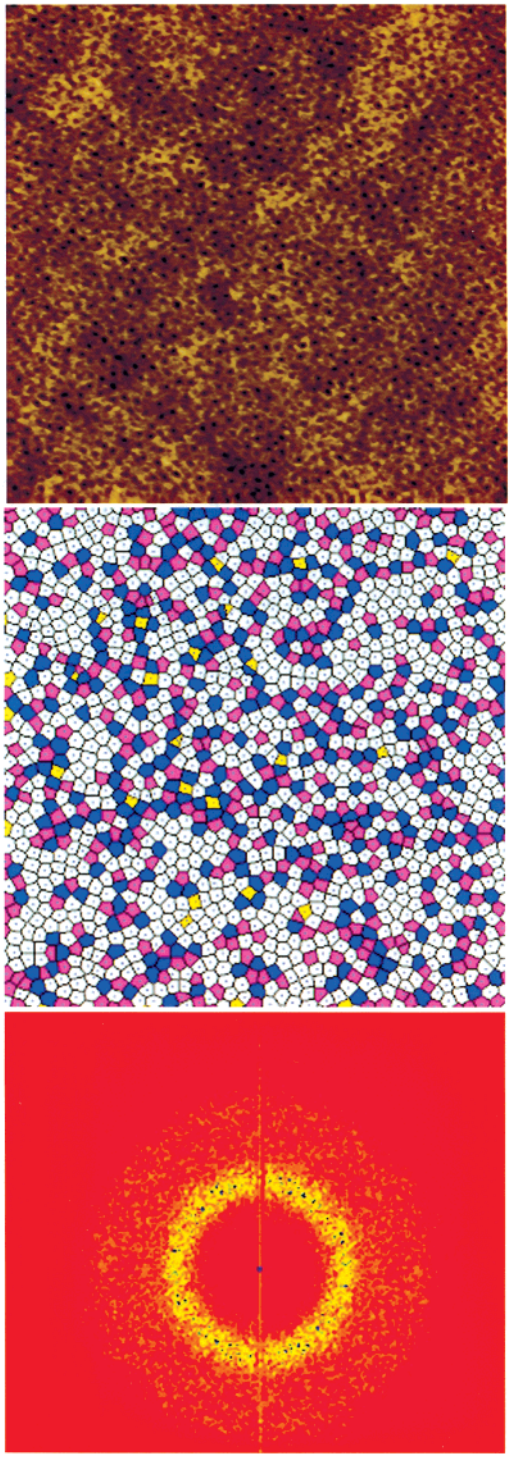

Figure 10. The PS−PVP diblock copolymer was annealed at 280 °C ($\chi N_{PVP} = 7.0$). Disclinations are no longer grouped into pairs and almost outnumber 6-fold coordinated sites. The Fourier transform depicts only a first-order ring, indicating that the system has melted into a liquid.

subsequent dislocation due to the effective screening of its strain field by others. At $\chi N_{PVP} = 7.2$ (264 °C), the defects are able to span across the whole image. Despite this large defect density, the six regions of higher intensity in the first-order ring of the Fourier transform indicate that the hexagonal symmetry is still retained at this point. Finally at $\chi N_{PVP} = 7$ (Figure 10), the system has melted into a liquid so that the Fourier transform shows a diffuse ring and the Voronoi diagram illustrates the presence of a few isolated dislocations with many disclination clusters spanning the width of the image.

This qualitative analysis indicates that a gradual melting transition occurs in the range of $7.5 > \chi N_{PVP} > 7.0$. It is useful to analyze the defects statistically in a larger number of SFM scans to carry the analysis further. Defect counts on a single 1.5 μm square SFM

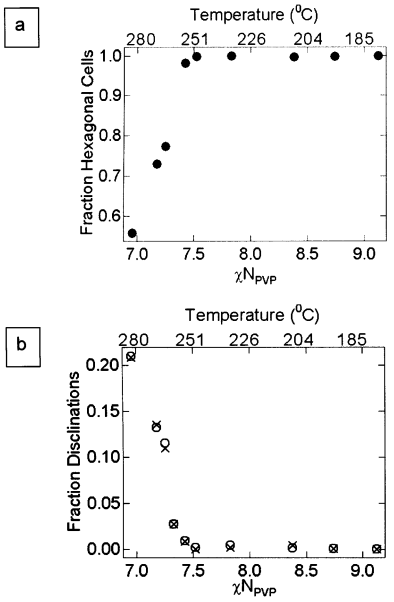

Figure 11. As temperature increases, the equilibrium number of dislocations should also increase and the fraction of 6-fold coordinated sites should decrease. (a) demonstrates that the change in number of hexagonal Voronoi cells is not noticeable until $\chi N_{PVP} = 7.5$ when dislocation pair proliferation becomes obvious. At this point the number of 6-fold sites decreases rapidly until they make up only half the spheres in the liquid state (at $\chi N_{PVP} = 7.0$ or 280 °C). (b) Fractions of +60° disclinations (7-fold coordinate sites) (open circles) and −60° disclinations (5-fold coordinate sites) (×'s).

scan containing ~2000 spheres yield only a very limited number. For the sake of statistical analysis, each sample was scanned at a minimum of five locations near the edge of a long (1 mm) mesa so as to gather a larger sample set (10 000 spheres). Figure 11a demonstrates that the fraction of spheres that are 6-fold coordinated (6's) is nearly unity for all $9.0 > \chi N_{PVP} > 7.5$. In this range, there are no grain boundaries within the 1.5 μm wide strip along the edge of the mesa, and the Fourier transform always indicates six very sharp diffraction peaks, indicating that we have a relatively defect-free crystal. As χN_{PVP} is decreased below 7.5, the frequency of 6's decreases continuously. Figure 11b demonstrates that as the frequency of Voronoi hexagons decreases, disclinations (5's and 7's) are introduced in their place. The proportion of 5's is always nearly equal to that of 7's, indicating that they are created in equal numbers. The melting transition, as observed through an increase in the defect density count and a broadening of the diffraction spots in the digital Fourier transforms, occurs in the range of $7.4 > \chi N_{PVP} > 7.1$, which corresponds to a temperature range of 250−270 °C for a block copolymer with $N_{PVP} = 86$. Only when the system is nearly melted ($7.2 > \chi N_{PVP}$) are significant numbers of 4's present. The continuous increase in disclinations and decrease in hexagonal Voronoi cells indicates that the generation of new defects is a continuous process, not an abrupt transition.

Figure 12 demonstrates that the two-dimensional block copolymer film annealed at $\chi N_{PVP} = 9$ has a very sharp, symmetric distribution of inter-sphere spacings, a, that is well fit by a Gaussian. This is what would be expected for a hexagonal 2-D crystal in which all spheres should be evenly spaced. As the system melts, the distribution broadens with a slight skewing to broader distributions, as demonstrated in Figure 12b,c.

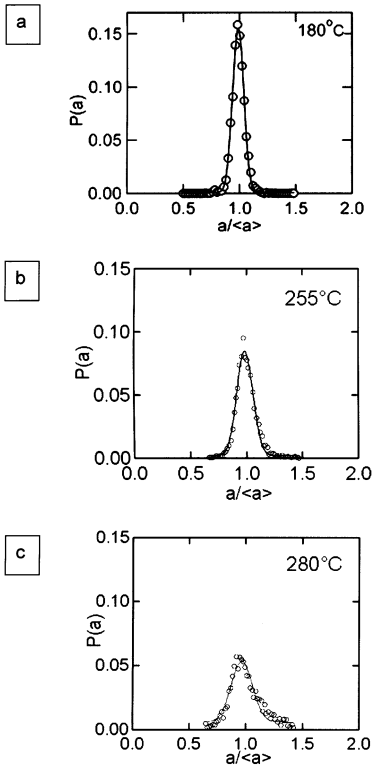

Figure 12. After 72 h at (a) 180 °C ($\chi N_{PVP} = 9.1$), the distribution of sphere spacings is quite narrow and symmetric and can be fit by a Gaussian (solid line). (b) $\chi N_{PVP} = 7.4$ (255 °C). As dislocations become more prominent, the distribution broadens and becomes slightly skewed toward larger sphere spacings. (c) $\chi N_{PVP} = 7.0$ (280 °C). When the system melts, the lattice spacing distribution is broadened significantly and is noticeably asymmetric.

The distribution of lattice spacings is a reflection of the local translational order of the system. At each temperature, for a sample set consisting of at least 10 000 spheres, the standard deviation, w, of the distribution was computed. The Lindemann criterion, originally formulated for 3-D systems, states that melting occurs when the root-mean-square displacement of the atoms, $\langle u(r)^2 \rangle^{1/2}$, from their nearest neighbors exceeds approximately $0.1a$. It has been suggested that this melting criterion is universal because it only accounts for changes in the local coordinates of the atoms. It is unaffected by the differences in long-range order of the 3-D vs the 2-D crystal and does not address the continuous nature of the 2-D transition.[51] For application to the two-dimensional case, however, the mean square of the difference between displacements of adjacent spheres, $\langle u(r + a) - u(r))^2 \rangle$, must be used since $\langle u(r)^2 \rangle$ diverges with system size. By definition, the standard deviation in lattice spacings, w, is related to this mean-square difference, $\langle u(r + a) - u(r))^2 \rangle = w^2$.[76]

The authors are wary to compare exact values of average sphere spacings between SFM images since the thermal drift of the piezo within the SFM makes these measurements variable within the 5% region of interest from scan to scan and from day to day. Within a single image, however, the measurements of $\langle a \rangle$ are very reliable, so it is possible to compare normalized standard deviations of sphere to sphere spacings. Figure 13 demonstrates that this distribution broadens continuously from the well-ordered case at $\chi N_{PVP} = 9$ all the way to the liquid state at $\chi N_{PVP} = 7.0$. Note that despite

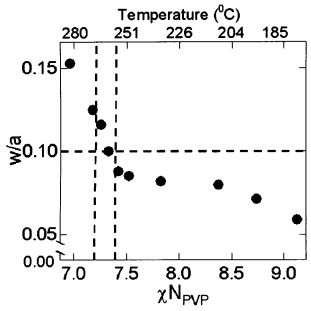

Figure 13. Standard deviation, w, of the sphere spacing distribution and its normalized value (w/a) change continuously throughout the range of χN_{PVP} observed, indicating that despite the fact that the defect count was stable in the range of $9.1 > \chi N_{PVP} > 7.5$, the degree of local translational order decreases with increasing temperature. The Lindemann criterion for melting is drawn as horizontal dashed line.

the fact that we observe a single crystal over the range $\chi N_{PVP} = 9$ to $\chi N_{PVP} = 7.5$, w/a increases constantly with increasing temperature, indicating that the crystal is becoming softer in this regime. The Lindemann criterion for melting ($w/a = 0.1$) is satisfied when $\chi N_{PVP} = 7.4$, though the distribution is seen to broaden significantly after this point. Despite the implication of the Lindemann criterion that melting is a first-order transition occurring when $w/a = 0.1$, our sphere spacing distribution changes smoothly around this region, indicating that the transition is a continuous one.

Translational and Orientational Order in 2-D. In a 2-D crystal phase, unlike the three-dimensional analogue, its long-range order is destroyed by thermally excited long wavelength phonons so conventional long-range translational order is impossible.[35] The two-dimensional crystal will have quasi-long-range translational order, and a pair correlation function will decay to 0 algebraically. At any temperature, the two-dimensional crystal in thermal equilibrium will also have some nonzero number of dislocation pairs, but the orientational order will be long range. As the temperature is increased, the concentration of free dislocations increases, making the crystal mechanically unstable leading to a continuous transition to the hexatic phase. In KTHNY theory, this transition occurs when the dimensionless combination of elastic constants, K, falls below the numeric value:

$$K = 4a^2\frac{\mu(\mu+\lambda)}{2\mu+\lambda} = 16\pi \qquad (4)$$

where μ and λ are the 2-D Lamé elastic constants normalized by k_bT where k_b is Boltzmann's constant and T is temperature. The presence of an increasing number of dislocations in the hexatic phase destroys the translational order so that a pair correlation function decays exponentially, but dislocations have much less effect on the orientational order. The quasi-long-range orientational order of the hexatic, however, is destroyed by the dislocation−disclination unbinding transition to an isotropic liquid.

The translational correlation function, $G_T(r)$, is useful for quantifying the range of the translational order in the system. $G_T(r)$ was calculated from the measured sphere center positions using $\exp(i\vec{K}\cdot\vec{r})$ as the order parameter:

$$G_T(r) = \langle e^{i\vec{K}\cdot\vec{r}'} e^{-(i\vec{K}\cdot(\vec{r}'-\vec{r}))}\rangle \qquad (5)$$

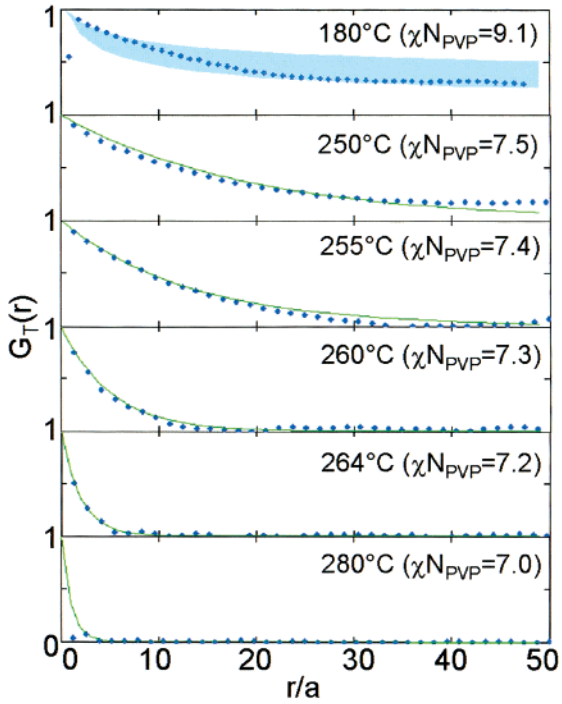

Figure 14. Representative translational correlation functions, $G_T(r)$ (●), at annealing conditions of 180, 250, 255, 260, 264, and 280 °C. The diblock copolymer annealed at 180 °C ($\chi N_{PVP} = 9.1$) fits well within the green shaded region representing expected algebraic decay of the quasi-long-range translational order in a crystal: $G_T(r) \sim r^{-\eta}$ where $0.33 > \eta > 0.25$. For 250−280 °C ($7.5 > \chi N_{PVP} > 7.0$), the data are fit with an exponential decay (solid line) to determine the translational correlation length, ξ_T. In this range translational order is short range.

where $\vec{K}$ is a reciprocal lattice vector to one of the first-order peaks in the 2-D Fourier transform and the brackets indicate an average over all spheres separated by $\vec{r}$ and an average over all six reciprocal lattice vectors. Each pair of spheres separated by $\vec{r}$ will have a translational order parameter, $\langle e^{i\vec{K}\cdot\vec{r}'} e^{(-i\vec{K}\cdot(\vec{r}'-\vec{r}))}\rangle$, with a value between 0 and 1. This translational correlation function is similar to a radial distribution function, which also measures translational order, but eq 5 allows us to compute the translational order out to a larger r in the same 1.5 μm square area since boundary conditions are not important.

True long-range order, as described by a $G_T(r) = 1$ for all r, is not possible for a real two-dimensional system as discussed above.[35] A real two-dimensional crystal is characterized by quasi-long-range translational order with a $G_T(r)$ which decays algebraically to 0 at large values of r, following the form

$$G_T(r) \propto \left(\frac{r}{a}\right)^{-\eta_T} \qquad (6)$$

where the distance, r, is normalized by the average sphere spacing, a, and η_T is a fitting parameter. Halperin and Nelson[39] predict that $G_T(r)$ for the ordered crystal phase should have a η_T in the range of $^1/_4$−$^1/_3$. As shown in Figure 14, a block copolymer thin film annealed under conditions such that $\chi N_{PVP} = 9.1$ has a $G_T(r)$ with a η_T that falls within this crystal range.

The quasi-long-range translational order of the 2-D crystal is destroyed by the generation of free dislocations from dislocation pair unbinding. As the concentration of free dislocations increases with temperature, there

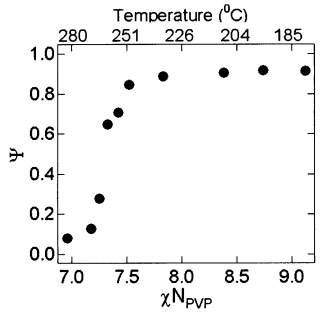

Figure 15. The local orientational order, Ψ, is maintained at very high levels (Ψ → 1) until the dislocation pair dissociation becomes prevalent (around $\chi N_{PVP} = 7.4$, $T = 255$ °C), in contrast to the local translational order (observed through the distribution of sphere spacings) which decayed steadily throughout this temperature range.

is a continuous transition to the hexatic phase. In both the hexatic and liquid phases, the translational order is short-range and decays exponentially:

$$G_T(r) \propto \exp\left(-\frac{r}{\xi_T}\right) \tag{7}$$

where ξ_T is the translational correlation length. As seen in Figure 14, when $\chi N_{PVP} = 7.4$ ($T = 255$ °C), $G_T(r)$ decays exponentially with a correlation length of $\xi_T = 14a$, where a is the average lattice spacing. The correlation length continues to decrease so that $\xi_T = 9a$ at $\chi N_{PVP} = 7.3$ ($T = 260$ °C) and $\xi_T = 4a$ at $\chi N_{PVP} = 7.2$ ($T = 264$ °C). As expected, the correlation length decreases to a value of $\xi_T = a$ as the hexatic melts to an isotropic liquid.

The orientational order is defined by the orientation of the sphere-to-sphere "bond" vectors. The local bond orientational order parameter is

$$\psi(r_{ij}) = \exp(6i\theta(r_{ij})) \tag{8}$$

where sphere j is a nearest-neighbor of sphere i and $\theta(r_{ij})$ is the angle made between the bond connecting spheres i and j and an arbitrarily chosen reference axis. The constant, 6, appears in the exponential to represent an invariance to rotation through $2\pi/6$. To find the local orientational order, this parameter may be autocorrelated:

$$\Psi = \left\langle \frac{\sum_{j}^{NN} \psi(r_{ij})\ \psi^*(r_{ij})}{NN} \right\rangle \tag{9}$$

where the index j counts the nearest neighbors, NN, of sphere i and the angular brackets denote an average over all spheres, N. The autocorrelation of the local orientational order parameter is the orientational order analogue of measuring bond length distributions. Ψ only averages local perturbations from the assumed hexagonal order, yielding a value of 1 for a perfectly hexagonal crystal and a value of 0 for an isotropic liquid. Figure 15 shows Ψ as a function of χN_{PVP} and T. It can be seen the level of local orientational order remains high to much lower χN_{PVP} (higher T) than does the local translational order (as seen in the bond length distributions). This is qualitatively what would be predicted by the KTHNY theory of melting in that the translational order appears to disappear at much lower temperature than does the orientational order.

Before the dislocation to disclination unbinding transition occurs, the orientational order is predicted to be quasi-long-range. The orientational correlation function is defined as

$$G_6(r) = \langle \psi^*_6(0)\ \psi_6(r) \rangle \tag{10}$$

where

$$\psi_6(r_i) = \frac{\sum_{j=1}^{NN} \exp(6i\theta(r_{ij}))}{NN} \tag{11}$$

and $\psi_6^*(0)$ indicates the complex conjugate of the order parameter of the sphere which is designated as the origin. Each sphere is used as the origin for one calculation, and the angular brackets indicate an average over all spheres. $G_6(r)$ has a value between 0 and 1 for all r. For a perfect hexagonal crystal, a plot of $G_6(r)$ vs r will have a value of 1 and will only exist when $r = na$, where n has a integer value. In a real crystal, the maximum value of this graph will not be 1.0 due to fluctuations in lattice positions even for a well ordered 2-D crystal. $G_6(r)$ will also appear to oscillate at low values of r since pairs of spheres separated by distances that are not an integral number of lattice spacings are by definition far out of optimal location and have low values of G_6. The rate and character of the decay of $G_6(r)$ with r are indicative of the degree of orientational order in the system.

Since orientational order is preserved through the initial stages of KTHNY melting, the orientational order of a 2-D crystal is long-range and is expected to decay only minimally so that $G_6(r)$ approaches a constant value as $r \to \infty$. The hexatic is expected to have quasi-long-range orientational order that can be fit to an algebraic function of the form

$$G_6(r) \propto \left(\frac{r}{a}\right)^{-\eta_\theta} \tag{12}$$

over the range of $0 < r < 40a$. The exponent, η_θ, is related to the Frank constant of the hexatic, K_A:

$$\eta_\theta = \frac{18k_bT}{\pi K_A} \tag{13}$$

The magnitude of K_A reflects the mechanical stability of the phase and is infinite in the crystal and zero in the liquid. $G_6(r)$ in a hexatic is expected to decay with a small exponent ($\eta_\theta \sim 0.1$). At the hexatic-to-liquid transition, the Halperin−Nelson analysis of the dislocation to disclination unbinding transition found that $K_A \to (72/\pi)k_bT$ so η_θ approaches 0.25.[39] In the isotropic liquid state, the short-range orientational order should decay exponentially.

Figure 16 shows $G_6(r)$ for a few representative values of χN_{PVP}. At $\chi N_{PVP} > 7.4$ ($T < 255$ °C), long-range orientational order is present so $G_6(r)$ decays little. At $\chi N_{PVP} = 7.4$, the orientational order is beginning to show signs of decay, though $\eta_\theta \sim 0.1$ indicating that it is only in the low-temperature region of the hexatic regime. A sample at $\chi N_{PVP} = 7.3$ has $\eta_\theta \sim 0.21$ and is very near the hexatic-to-liquid transition. The sample annealed at $\chi N_{PVP} = 7.2$ has $\eta_\theta \sim 0.50$, indicating that it has

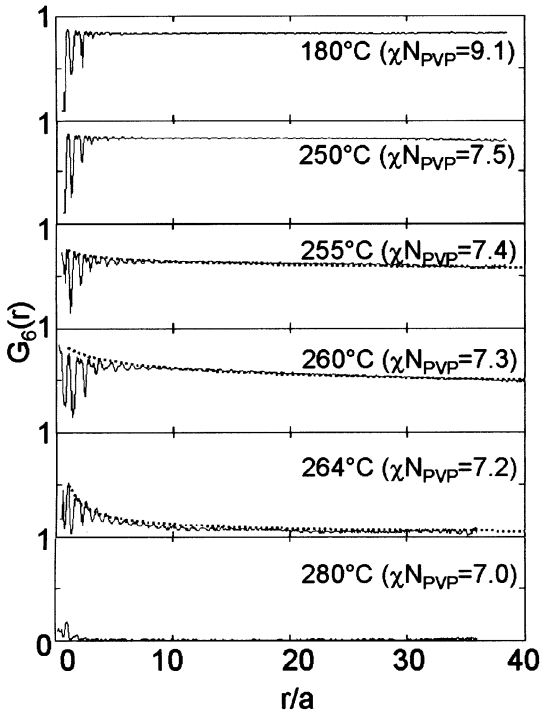

Figure 16. Representative orientational order correlation functions, $G_6(r)$ (solid lines), for annealing conditions of 180, 250, 255, 260, 264, and 280 °C. The most ordered systems (180 and 250 °C) show very little decay in orientational order even at very large distances ($r = 50a$). When the system is hexatically ordered, however, $G_6(r)$ decays algebraically as in eq 11 (dashed line) with $\eta_\theta = 0.1$, 0.21, and 0.5 respectively for 255, 260, and 264 °C. At 280 °C, the film is disordered and the decay of the $G_6(r)$ is exponential.

passed Halperin−Nelson orientational order definition of the liquid/hexatic transition, though Figure 9 presented earlier demonstrated that this system is still not truly liquid in that the Fourier transform and Voronoi diagram still demonstrated some hexagonal order. This indicates that the Halperin−Nelson criterion for the liquid/hexatic transition may be too restrictive. For sample annealed at $\chi N_{PVP} = 7.0$, the decay is exponential with a correlation length $= 1a$.

In Figure 17, the correlation lengths ξ_T and ξ_6 determined from the calculated translational and correlation functions are shown as a function of χN_{PVP}. To establish correlation lengths, both correlation functions were fit to exponentials of the form

$$G(r) \propto \exp\left(-\frac{r}{\xi}\right) \tag{14}$$

In each case, the correlation lengths are the result of averaging over a minimum of five SFM micrographs of different regions on a 1 mm long mesa so as to gain large statistics on which to base this analysis. Though in the case of translational order in the crystal and orientational order in the crystal and hexatic, the decay of the correlation function was really algebraic; a rough fit for $r < 15a$ with eq 10 was used to determine an approximate correlation length.

As expected, in all cases the orientational correlation length was larger than the translational correlation length since it is not as affected by the appearance of individual dislocations. Like the local order parameter results presented previously, both correlation lengths decrease continuously throughout the range of $7.5 < \chi N_{PVP} < 7.0$ (255−280 °C), indicating that the melting transition is a continuous process. At $\chi N_{PVP} = 7.4$, the translational correlation length (ξ_T) has decreased (by a factor of 2) from its approximate value for the 2-D crystal, indicating that the presence of dislocations and dislocation clusters is now affecting this form of order. The orientational correlation length (ξ_6) also drops at this point, but by a far less significant amount, indicating that orientational order is being preserved during this step. At $\chi N_{PVP} = 7.1$ (268 °C), the system appears to be in the liquid state (Fourier transform shows an isotropic ring), but $\xi_T = 1.5a$ and $\xi_6 = 3a$. Only when $\chi N_{PVP} = 7.0$ do the two correlation lengths coincide at $\xi_T = \xi_6 = 1a$.

All correlations used to define order in this paper (defect counts, sphere spacing distributions, local order correlation functions, and translational and orientational order correlation functions) indicate that the melting phenomenon is continuous. At no point did any of these factors change abruptly, indicating the presence of a first-order transition. There was also no temperature at which the crystalline and liquid phases appeared to coexist, as would be expected in a first-order transition. We conclude that melting in this 2-D system occurs through a continuous process with the crystal-to-hexatic transition occurring when $\chi N_{PVP} = 7.4$ (255 °C) and then meets the Halperin−Nelson criteria for the hexatic-to-liquid transition when $\chi N_{PVP} = 7.25$ (262 °C). This raises into question the definition of the hexatic phase with quasi-long-range orientational order evident in the 6-fold symmetry of a diffraction pattern of a finite size region. This degree of orientational order is still present in our system after the Halperin−Nelson−Young criteria, which predicts the dislocation unbinding transition (step 3 in Figure 3) has been satisfied.

The solid, hexatic, and liquid phase boundaries are drawn as gray vertical lines in Figure 13 describing the changes in sphere spacing distributions. The Lindemann criterion ($w/a = 0.1$) is satisfied at $\chi N_{PVP} = 7.3$ (260 °C), near the hexatic-to-liquid transition. Seshadri and Westervelt obtained a similar result for the hexatic-to-liquid transition in their study of the melting of 2-D magnetic bubble arrays.[62] This is of particular interest since in the magnetic bubbles, like the block copolymer spheres, can deform and change size during the melting process.

From the SFM scans, it is possible to fully characterize the defects in a two-dimensional lattice of block copolymer spheres. Furthermore, we have been able to show that this two-dimensional lattice melts in a manner conforming to the defect-mediated phenomenon proposed in the KTHNY theory. Through analysis of the translational and orientational order, sphere-to-sphere spacing distribution, and local orientational order correlation functions, we have demonstrated that this transition from crystal to hexatic to liquid is continuous. At all $\chi N_{PVP} > 7.4$ ($T < 255$ °C), the system retains long-range orientational and quasi-long-range translational order and fits the profile of a 2-D crystalline solid. In the hexatic regime, $7.4 > \chi N_{PVP} > 7.25$, the system demonstrates quasi-long-range orientational order, but the translational order is now short-ranged. The system finally melts at $\chi N_{PVP} = 7.2$ to a liquid with short-range orientational and translational order.

3-Dimensional Melting. Very thick films of sphere forming layers present an interesting intermediate between three-dimensional bulk samples and the two-dimensional case of thin films consisting of a single layer

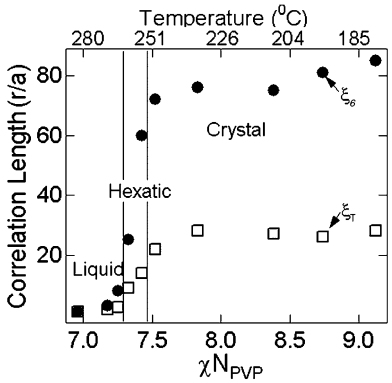

Figure 17. Comparison of translational correlation lengths ($\xi_T \rightarrow \square$) and orientational correlation lengths ($\xi_6 \rightarrow \bullet$). For the purposes of calculating correlation lengths, all correlation functions were fit with exponentials of the form of eq 12. In cases where quasi-long-range order existed (translational order in a crystal regime and orientational order in the crystal and hexatic regimes), the decay was algebraic, and this fit was only possible over the first $10a-20a$ and was necessarily poor, but was used regardless to give approximate correlation lengths. For $\chi N_{PVP} > 7.4$, the system is a 2-D crystal, for $7.4 > \chi N_{PVP} > 7.25$, the system is hexatic, and for $\chi N_{PVP} < 7.2$, the system is liquid. In all cases except the liquid, the orientational order persists over much larger distances than does the translational order.

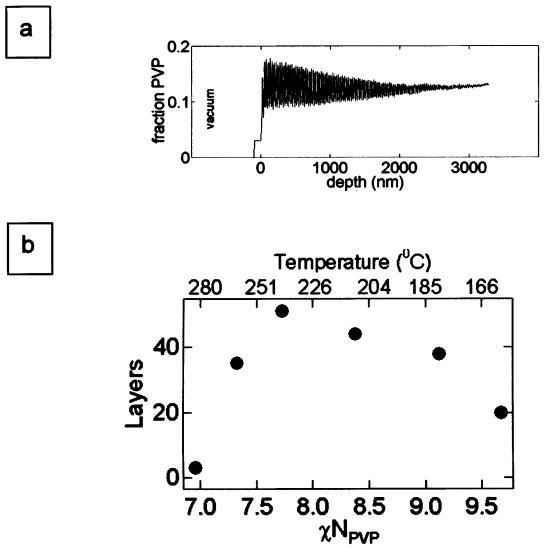

Figure 18. Layering in thick PS−PVP films. (a) A SIMS depth profile of the volume fraction of PVP of a PS−PVP 10 μm thick film after annealing for 24 h at 240 °C ($\chi N_{PVP} = 7.75$) at $P < 10^{-5}$ Torr and then quenching to room temperature. Each peak corresponds to a close-packed layer of PVP spheres. (b) Temperature dependence of the range of the layered structure induced by a vacuum surface. The last layer is defined as that which has half the maximum amplitude of oscillation.

of spheres discussed earlier in this paper. Yokoyama et al. demonstrated that in these thick films close-packed layers of spheres stack from both the vacuum surface and substrate surface in a manner similar to graphoepitaxy in two dimensions.[27] As mentioned previously, an interplay between block copolymer kinetics and thermodynamics controls the extent to which layers of spheres stack with registry to the surface. Using the same PS−PVP polymer, Yokoyama et al. therefore found that an optimum in layer stacking can be observed when $\chi N_{PVP} = 9$ ($T = 180$ °C) when the sample was annealed for 24 h at vacuum ($P \sim 10^{-3}$ Torr) and then quenched to room temperature for SIMS profiling. We have repeated these studies under the same vacuum conditions as used in the 2-D melting studies ($P < 10^{-6}$ Torr).

As presented in Figure 18a, the stacking of close-packed layers of spheres is observed in the SIMS as an oscillation in the mass = 26 (CN^-) signal which is an indicator for PVP. In Figure 18a, the mass = 26 signal has been converted to fraction PVP by means of a simple mass balance and is presented as a depth profile from the free surface. The oscillations decay with depth as the surface-induced stacking effect diminishes deep within the 10 μm thick film. It is difficult to reliably measure the number of peaks in the SIMS depth profile more than 1.5 μm below the surface due to the broadening of the instrumental resolution function of SIMS with depth. Instead, we will use the number of oscillations prior to the depth at which the amplitude of the oscillation becomes half of the maximum amplitude as an indication of the degree to which the surface has an effect on the stacking of close-packed layers. In Figure 18b, we find that the optimum annealing conditions in thick films are strikingly similar to the 2-D thin film case discussed previously. An optimum annealing condition exists at $\chi N_{PVP} = 7.75$ ($T = 240$ °C) when more than 90 layers are seen stacking from the surface. At lower temperatures fewer layers are stacked which we believe indicates that the system is kinetically trapped. In the 2-D analogue, $\chi N_{PVP} = 7.75$ ($T = 240$ °C) was at the high-temperature end of the solid regime. At the next higher temperature step, $\chi N_{PVP} = 7.3$ ($T = 260$ °C), a significant decrease in the number of stacked layers is seen. In 2-D studies, these annealing conditions, $\chi N_{PVP} = 7.3$ ($T = 260$ °C), yielded hexatic order. At $\chi N_{PVP} = 7.0$ ($T = 280$ °C), only short-range surface-induced layering is observed.

The discrepancy in temperature between these results and those presented by Yokoyama et al. can be attributed to the difference in vacuum conditions of annealing. At temperatures greater than 200 °C, the PS−PVP diblock copolymer is more susceptible to thermal degradation in the poor vacuum used by Yokoyama et al. In these conditions, significant chain scission may occur, resulting in a disordering of the block copolymer sphere lattice. This entire process occurs without any visible change to the polymer film when studied via optical microscopy, SIMS, or SFM.

The bulk T_{LDOT} of a block copolymer is not necessarily expected to coincide with the 2-D melting temperature because the 2-D system is more susceptible to the disordering effects of fluctuations than the 3-D block copolymer. Figure 19a shows a SAXS pattern from the 3-D bulk block copolymer sample (sample thickness = 0.8 mm) at $\chi N_{PVP} = 7.0$ (280 °C) during the heating cycle, clearly demonstrating q^* and $2^{1/2}q^*$ rings. Figure 20a shows azimuthally averaged 2-D SAXS profiles for the bulk sample of PS−PVP diblock copolymer measured in situ at various temperatures during the heating and cooling protocol described previously. At $\chi N_{PVP} \geq 7.0$ ($T \leq 280$ °C), the scattering maxima exist at relative peak positions of $2^{1/2}q^*$ and $3^{1/2}q^*$. These higher-order scattering peaks indicate the presence of a body-centered-cubic lattice of spheres (bcc spheres). When the temperature is raised to $\chi N_{PVP} = 6.6$ (300 °C) (Figure 19b), the $2^{1/2}q^*$ ring disappears, suggesting the presence of a disordered sphere phase. Upon cooling to $\chi N_{PVP} = 6.8$ (290 °C), the higher-order peaks reappear as a broad shoulder ranging from 0.3 to 0.5 nm^{-1} (Figure 20).

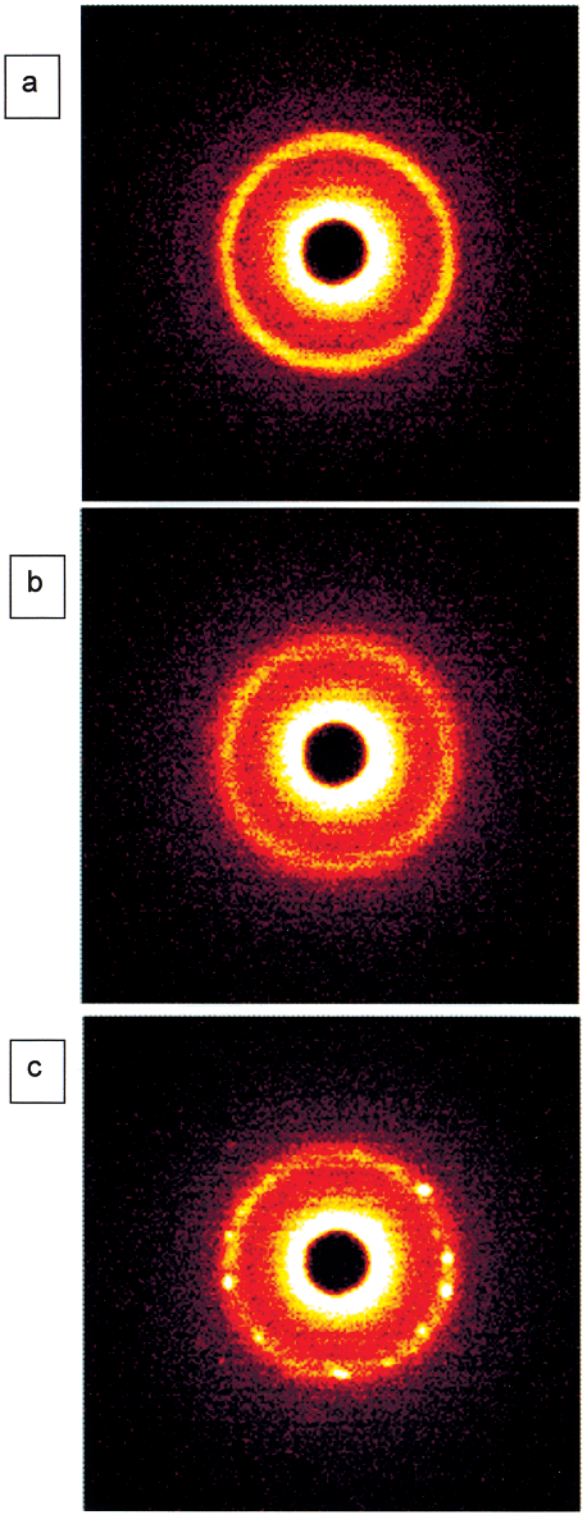

Figure 19. (a) 2-D SAXS pattern generated from a sample at 280° C ($\chi N_{PVP} = 7.0$) during the heating cycle. Both the q^* ring and $2^{1/2}q^*$ ring are clearly visible. (b) At 300 °C ($\chi N_{PVP} = 6.6$), the $2^{1/2}q^*$ has disappeared. (c) When cooled to 290 °C ($\chi N_{PVP} = 6.8$), definite peaks are present in the q^* ring, indicating the presence of very large grains of crystalline structure.

Though the presence of the $2^{1/2}q^*$ ring is not obvious in Figure 19c, distinct peaks are observed in the q^* ring, indicating that some long-range order has reappeared.[77]

A plot of the reciprocal of the first-order peak intensity ($I^{-1}(q^*)$) vs χN_{PVP} (and temperature) in Figure 20b reveals a discontinuity in slope between $\chi N_{PVP} = 6.8$ and 6.6 (290 and 300 °C). These data indicate that the T_{LDOT} occurs in somewhere in this range. Data points from heating and cooling cycles fall on the same line, indicating that the transition was reversible (as expected) and that no oxidation or degradation occurred in the polymer during the thermal cycling process. Unfortunately, when the temperature is increased above 300 °C, the viscosity of the polymer becomes so low that it flows out of the heat cell, so it was impossible to achieve any higher temperatures or more exactly measure T_{LDOT} in this study. The SAXS data show clearly that melting of the 3-D block copolymer (LDOT) occurs at a significantly higher temperature (~290 °C) than the hexatic-to-isotropic liquid transition of the 2-D block copolymer film. This somewhat surprising result suggests that the 2-D liquid of disordered micelles is more strongly stabilized by fluctuations than is the corresponding 3-D micelle fluid.

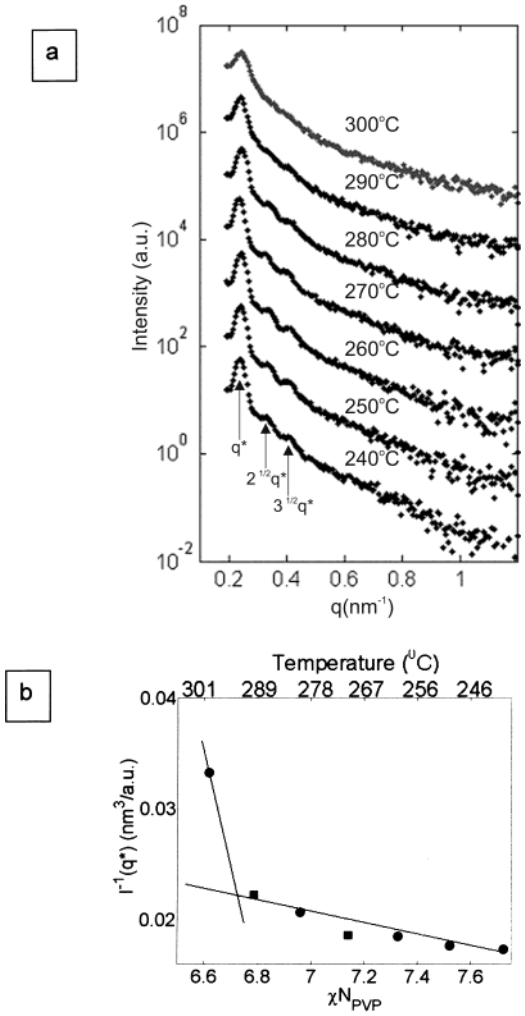

Figure 20. Temperature dependence of SAXS profiles for PS–PVP diblock copolymer at various temperatures ranging from 240 to 300 °C. (a) All profiles are azimuthal averages of 2-D SAXS patterns. The intensities of the SAXS profile at 240 °C are measured values while each subsequent set has been shifted up by 1 decade relative to the set below. At 290 °C ($\chi N_{PVP} = 6.8$) the $2^{1/2}q^*$ and $3^{1/2}q^*$ peaks blend into a broad shoulder, and at 300 °C they are not visible at all. (b) Plots of $I^{-1}(q^*)$ vs χN_{PVP} (and temperature) during the heating (circles) and cooling (squares) processes. A change in slope of $I^{-1}(q^*)$ vs χN_{PVP} around 290 °C ($\chi N_{PVP} = 6.8$) indicates the approximate position of the T_{LDOT}.

Conclusions

From the quantitative analysis of order via defect counts, lattice spacing distributions, and order correlation functions, it was obvious that a 2-D block copolymer crystal melts continuously through the generation and unbinding of dislocation pairs at low temperatures followed by the unbinding of the dislocations into their constituent disclinations at higher temperatures. When $\chi N_{PVP} > 7.4$, a 2-D crystal with long-range orientational and quasi-long-range translational order was observed, but when $7.4 \geq \chi N_{PVP} \geq 7.25$ translational order was disrupted to yield a hexatic phase with quasi-long-range orientational order but short-range translational order. At still higher temperatures ($\chi N_{PVP} < 7.2$) orientational order also decayed, leading to a liquid state with short-range orientational and translational order. In a thick film, the range of layering of block copolymer spheres from the surface follows a similar temperature dependence, and a maximum in this range is observed when $\chi N_{PVP} = 7.75$ ($T = 240$ °C). We observe the 3-D bulk T_{LDOT} occurs at a χN_{min} 0.3 higher than that of the hexatic to 2-D liquid transition. To obtain a 2-D crystal with best order, annealing at temperatures close to but below the 2-D crystal to hexatic transition is the best strategy since at such temperatures, the kinetics of ordering are rapid but the thermal defect generation is not significant. Even if defects are eliminated by such annealing, however, it will not be possible to achieve 2-D block copolymer crystals with long-range translational order by unassisted self-assembly. These limitations must be considered when using block copolymer films for nanolithographic applications.

Acknowledgment. We gratefully acknowledge the financial support of the U.S. National Science Foundation DMR Polymers Program under Grant DMR 98-03738, MRSEC Program under Award DMR 00-80034 for support of A.H., and the Corning Foundation for fellowship support of R.A.S. Helpful discussions with Glenn Fredrickson, David Nelson, Hideaki Yokoyama, Patrick Davidson, and Sergei Magonov as well as the assistance of Tom Mates for SIMS are greatly appreciated.

References and Notes

(1) Park, M.; Harrison, C.; Chaikin, P. M.; Register, R. A.; Adamson, D. H. *Science* **1997**, *276*, 1401−1404.
(2) Li, R. R.; Dapkus, P. D.; Thompson, M. E.; Jeong, W. G.; Harrison, C.; Chaikin, P. M.; Register, R. A.; Adamson, D. H. *Appl. Phys. Lett.* **2000**, *76*, 1689−1691.
(3) Guarini, K. W.; Black, C. T.; Milkove, K. R.; Sandstrom, R. L. *J. Vac. Sci. Technol. B* **2001**, *19*, 2784−2788.
(4) Black, C. T.; Guarini, K. W.; Milkove, K. R.; Baker, S. M.; Russell, T. P.; Tuominen, M. T. *Appl. Phys. Lett.* **2001**, *79*, 409−411.
(5) Cheng, J. Y.; Ross, C. A.; Chan, V. Z. H.; Thomas, E. L.; Lammertink, R. G. H.; Vancso, G. J. *Adv. Mater.* **2001**, *13*, 1174−1178.
(6) Kim, H. C.; Jia, X. Q.; Stafford, C. M.; Kim, D. H.; McCarthy, T. J.; Tuominen, M.; Hawker, C. J.; Russell, T. P. *Adv. Mater.* **2001**, *13*, 795−797.
(7) Thurn-Albrecht, T.; Schotter, J.; Kastle, C. A.; Emley, N.; Shibauchi, T.; Krusin-Elbaum, L.; Guarini, K.; Black, C. T.; Tuominen, M. T.; Russell, T. P. *Science* **2000**, *290*, 2126−2129.
(8) Sohn, B. H.; Seo, B. H. *Chem. Mater.* **2001**, *13*, 1752−1757.
(9) Watkins, J. J.; McCarthy, T. J. *Chem. Mater.* **1995**, *7*, 1991−1999.
(10) Mansky, P.; DeRouchey, J.; Russell, T. P.; Mays, J.; Pitsikalis, M.; Morkved, T.; Jaeger, H. *Macromolecules* **1998**, *31*, 4399−4401.
(11) Morkved, T. L.; Lu, M.; Urbas, A. M.; Ehrichs, E. E.; Jaeger, H. M.; Mansky, P.; Russell, T. P. *Science* **1996**, *273*, 931−933.
(12) Huang, E.; Russell, T. P.; Harrison, C.; Chaikin, P. M.; Register, R. A.; Hawker, C. J.; Mays, J. *Macromolecules* **1998**, *31*, 7641−7650.
(13) Mansky, P.; Russell, T. P.; Hawker, C. J.; Pitsikalis, M.; Mays, J. *Macromolecules* **1997**, *30*, 6810−6813.
(14) Heier, J.; Genzer, J.; Kramer, E. J.; Bates, F. S.; Walheim, S.; Krausch, G. *J. Chem. Phys.* **1999**, *111*, 11101−11110.
(15) Yang, X. M.; Peters, R. D.; Nealey, P. F.; Solak, H. H.; Cerrina, F. *Macromolecules* **2000**, *33*, 9575−9582.
(16) Peters, R. D.; Yang, X. M.; Nealey, P. F. *Macromolecules* **2002**, *35*, 1822−1834.
(17) Segalman, R. A.; Yokoyama, H.; Kramer, E. J. *Adv. Mater.* **2001**, *13*, 1152−1155.
(18) Yokoyama, H.; Mates, T. E.; Kramer, E. J. *Macromolecules* **2000**, *33*, 1888−1898.
(19) Yokoyama, H.; Kramer, E. J. *Macromolecules* **1998**, *31*, 7871−7876.
(20) Lodge, T. P.; Blazey, M. A.; Liu, Z.; Hamley, I. W. *Macromol. Chem. Phys.* **1997**, *198*, 983−995.
(21) Kim, W. G.; Garetz, B. A.; Newstein, M. C.; Balsara, N. P. *J. Polym. Sci., Part B: Polym. Phys.* **2001**, *39*, 2231−2242.
(22) Han, C. D.; Vaidya, N. Y.; Kim, D.; Shin, G.; Yamaguchi, D.; Hashimoto, T. *Macromolecules* **2000**, *33*, 3767−3780.
(23) Sakamoto, N.; Hashimoto, T.; Han, C. D.; Kim, D.; Vaidya, N. Y. *Macromolecules* **1997**, *30*, 1621−1632.
(24) Sakamoto, N.; Hashimoto, T. *Macromolecules* **1998**, *31*, 8493−8502.
(25) Adams, J. L.; Graessley, W. M.; Register, R. A. *Macromolecules* **1994**, *27*, 6026−6032.
(26) Adams, J. L.; Quiram, D. J.; Graessley, W. W.; Register, R. A.; Marchand, G. R. *Macromolecules* **1996**, *29*, 2929−2938.
(27) Yokoyama, H.; Kramer, E. J.; Rafailovich, M. H.; Sokolov, J.; Schwarz, S. A. *Macromolecules* **1998**, *31*, 8826−8830.
(28) Schwab, M.; Stuhn, B. *Phys. Rev. Lett.* **1996**, *76*, 924−927.
(29) Schwab, M.; Stuhn, B. *Colloid Polym. Sci.* **1997**, *275*, 341−351.
(30) Bates, F. S.; Fredrickson, G. H. *Annu. Rev. Phys. Chem.* **1990**, *41*, 525−557.
(31) Dormidontova, E. E.; Lodge, T. P. *Macromolecules* **2001**, *34*, 9143−9155.
(32) Semenov, A. N. *Macromolecules* **1989**, *22*, 2849−2851.
(33) Landau, L. D. *Phys. Z. Sowjetunion* **1937**, *11*, 26−47.
(34) Peierls, R. E. *Ann. Institut H. Poincare* **1935**, *5*, 177−222.
(35) Mermin, N. D. *Phys. Rev.* **1968**, *176*, 250−254.
(36) Jancovici, B. *Phys. Rev. Lett.* **1967**, *19*, 20−22.
(37) Kosterlitz, J. M.; Thouless, D. J. *J. Phys. C: Solid State Phys.* **1973**, *6*, 1181−1203.
(38) Kosterlitz, J. M.; Thouless, D. J. *J. Phys. C: Solid* **1972**, L124−126.
(39) Halperin, B. I.; Nelson, D. R. *Phys. Rev. Lett.* **1978**, *41*, 121−124.
(40) Nelson, D. R.; Halperin, B. I. *Phys. Rev. B* **1979**, *19*, 2457−2484.
(41) Young, A. P. *Phys. Rev. B* **1979**, *19*, 1855−1866.
(42) Sinha, S. K. *Ordering in two dimensions: proceedings of an international conference held at Lake Geneva, Wisconsin, U.S.A.; May 28−30, 1980*; North-Holland: New York, 1980.
(43) Strandburg, K. J. *Rev. Mod. Phys.* **1988**, *60*, 161−207.
(44) Kalia, R. K.; Vashishta, P. *J. Phys. C: Solid State Phys.* **1981**, *14*, L643−648.
(45) Kalia, R. K.; Vashishta, P.; de Leeuw, S. W. *Phys. Rev. B: Condens. Matter* **1981**, *23*, 4794−4797.
(46) Bedanov, V. M.; Gadiyak, G. V.; Lozovik, Y. E. *Phys. Lett. A* **1982**, *92A*, 400−402.
(47) Bagchi, K.; Andersen, H. C.; Swope, W. *Phys. Rev. E* **1996**, *53*, 3794−3803.
(48) Jaster, A. *Phys. Rev. E* **1999**, *59*, 2594−2602.
(49) Schweigert, I. V.; Schweigert, V. A.; Peeters, F. M. *Phys. Rev. Lett.* **2000**, *84*, 4381−4384.
(50) Bladon, P.; Frenkel, D. *Phys. Rev. Lett.* **1995**, *74*, 2519−2522.
(51) Zheng, X. H.; Earnshaw, J. C. *Europhys. Lett.* **1998**, *41*, 635−640.
(52) Fernandez, J. F.; Alonso, J. J.; Stankiewicz, J. *Phys. Rev. Lett.* **1995**, *75*, 3477−3480.
(53) Fernandez, J. F.; Alonso, J. J.; Stankiewicz, J. *Phys. Rev. Lett.* **1997**, *78*, 399−399.
(54) Weber, H.; Marx, D. *Phys. Rev. Lett.* **1997**, *78*, 398−398.
(55) Murray, C. A.; Van Winkle, D. H. *Phys. Rev. Lett.* **1987**, *58*, 1200−1203.

(56) Van Winkle, D. H.; Murray, C. A. *J. Chem. Phys.* **1988**, *89*, 3885−3891.
(57) Murray, C. A.; Sprenger, W. O.; Wenk, R. A. *Phys. Rev. B: Condens. Matter* **1990**, *42*, 688−703.
(58) Murray, C. A.; Van Winkle, D. H.; Wenk, R. A. *Phase Transitions* **1990**, *21*, 93−126.
(59) Marcus, A. H.; Rice, S. A. *Phys. Rev. Lett.* **1996**, *77*, 2577−2580.
(60) Marcus, A. H.; Rice, S. A. *Phys. Rev. E* **1997**, *55*, 637−656.
(61) Zahn, K.; Lenke, R.; Maret, G. *Phys. Rev. Lett.* **1999**, *82*, 2721−2724.
(62) Seshadri, R.; Westervelt, R. M. *Phys. Rev. B: Condens. Matter* **1992**, *46*, 5150−5161.
(63) Seshadri, R.; Westervelt, R. M. *Phys. Rev. B: Condens. Matter* **1992**, *46*, 5142−5149.
(64) Chui, S. T. *Ann. Phys.* **1973**, *80*, 361−386.
(65) Chou, T.; Nelson, D. R. *Phys. Rev. E* **1996**, *53*, 2560−2570.
(66) Karnchanaphanurach, P.; Lin, B. H.; Rice, S. A. *Phys. Rev. E* **2000**, *61*, 4036−4044.
(67) Angelescu, D.; Harrison, C.; Trawick, M.; Sebastian, J.; Chaikin, P. M.; Register, R. A.; Adamson, D. H. In *Bulletin of the American Physical Society March Meeting*: Indianapolis, IN, 2002; Vol. 47, Part II, p 900.
(68) Segalman, R. A.; Schaefer, K.; Magonov, S.; Kramer, E. J. *Macromolecules*, in press.
(69) Pradere, P.; Thomas, E. L. *Ultramicroscopy* **1990**, *32*, 149−168.
(70) Allen, S. M.; Thomas, E. L. *The Structure of Materials*; J. Wiley: New York, 1999.
(71) Chaikin, P. M.; Lubensky, T. C. *Principles of Condensed Matter Physics*, 1st pbk. ed.; Cambridge University Press: New York, 2000.
(72) Pertsinidis, A.; Ling, X. S. *Phys. Rev. Lett.* **2001**, *8709*, 8303, U8145−U8147.
(73) Trawick, M.; Angelscu, D.; Chaikin, P. M.; Sebastian, J.; Register, R.; Adamson, D.; Harrison, C. In *Bulletin of the American Physical Society March Meeting*: Indianapolis, IN, 2002; Vol. 47, Part II.
(74) Segalman, R. A.; Hexemer, A.; Kramer, E. J. *Macromolecules*, in press.
(75) Trawick, M.; Angelscu, D.; Chaikin, P. M.; Sebastian, J.; Register, R.; Adamson, D.; Harrison, C. In *Bulletin of the American Physical Society March Meeting*: Indianapolis, IN, 2002; Vol. 47, Part II, p 970.
(76) Bedanov, V. M.; Gadiyak, G. V.; Lozovik, Y. E. *Phys. Lett. A* **1985**, *109*, 289−291.
(77) The presence of these first-order peaks indicates that very large grains have grown from the melt. The fast growth of large grains of lamellar and cylindrical block copolymer structures from the disordered state is well documented.[23,73,74] We can gain a rough estimate of the grain size by considering that the interaction volume is $\sim$1 mm^3 (beam spot is approximately 1 mm $\times$ 1 mm), and there are on order 10−100 spots in the diffraction pattern, which would give a linear dimension of about 200−500 μm for the grains. There is some background intensity in the isotropic ring whose intensity is only half that of the 280 °C sample. This indicates that 50% of the polymer is still disordered due to either kinetic effects (not enough annealing time after quenching from TLDOT) or some phase coexistence of the disordered and ordered spherical phases.
(78) Newstein, M. C.; Garetz, B. A.; Balsara, N. P.; Chang, M. Y.; Dai, H. J. *Macromolecules* **1998**, *31*, 64−76.
(79) Lodge, T. P.; Pudil, B.; Hanley, K. J. *Macromolecules* **2002**, *35*, 4707−4717.

MA021367M